Results in Engineering 30 (2026) 110850

Contents lists available at ScienceDirect

Results in Engineering

journal homepage: www.sciencedirect.com/journal/results-in-engineering

Research paper

Non-destructive testing of CFRP laminates for aerospace structures: Acoustic emission and ultrasonic longitudinal wave (ULW) evaluation under Mode II loading with destructive validation

Muhammad Akhsin Muflikhun [a,b,*], Bodo Fiedler [c]

[a] Mechanical and Industrial Engineering Department, Universitas Gadjah Mada (UGM), Indonesia
[b] Center of Energy Studies, Universitas Gadjah Mada (UGM), Indonesia
[c] Institute of Composite and Polymer, Hamburg University of Technology (TU Hamburg), Germany

ARTICLE INFO

Keywords:
NDT evaluation
ENF
Acoustic emission
Ultrasonic longitudinal wave
Composite Laminates

ABSTRACT

Carbon Fiber Reinforced Polymer (CFRP) laminates are widely used in aerospace structures. However, understanding their damage mechanisms under Mode II loading and establishing reliable non-destructive testing (NDT) techniques remain critical challenges for structural health monitoring. This study investigates the fracture behavior and damage evolution of thin CFRP laminates with two stacking sequences, $[0°/+45°/-45°]_{2S}$ and $[+45°/-45°/0°]_{2S}$, using End-Notched Flexure (ENF) testing combined with Acoustic Emission (AE) and Ultrasonic Longitudinal Wave (ULW) evaluation. The results show that the $[0°/+45°/-45°]_{2S}$ laminates exhibit higher flexural stiffness and delayed crack initiation with sudden catastrophic crack propagation, whereas the $[+45°/-45°/0°]_{2S}$ laminates demonstrate earlier crack initiation and more progressive crack growth during loading. The average Mode II interlaminar fracture toughness values were approximately 1.70 kJ/m² for $[0°/+45°/-45°]_{2S}$, and 1.78 kJ/m² for $[+45°/-45°/0°]_{2S}$, indicating that stacking sequence significantly influences delamination resistance and energy dissipation. AE signal parameters, including absolute energy, duration, and average frequency, reveal distinct damage evolution stages, while ultrasonic scanning confirms different damage distributions where $[0°/+45°/-45°]_{2S}$ laminates show broader delamination zones and $[+45°/-45°/0°]_{2S}$ laminates exhibit more localized defects. This study provides valuable insights into the structural health monitoring of aerospace composite structures and demonstrates the potential of integrated NDT systems for developing damage-detection methods for advanced lightweight composite components.

1. Introduction

Recent studies on Carbon Fiber Reinforced Polymer (CFRP) laminates have increasingly focused on enhancing mechanical performance through targeted material and interface engineering strategies, as well as advancing experimental and analytical approaches to better understand failure mechanisms [1–3]. Advanced strategies primarily involve matrix and interface engineering, including hierarchical reinforcement and nano-modification approaches. For example, hierarchical CFRP composites have demonstrated significant improvements in interlaminar fracture toughness (Mode I: +168 %, Mode +155 %) through tailored microstructural design and controlled damage mechanisms [4,5]. In addition, hybrid nanoparticle systems such as graphene–TiO_2 have been shown to enhance tensile and flexural performance by improving interfacial load transfer and energy dissipation [6]. Complementarily, surface treatment techniques such as atmospheric plasma activation (APA) effectively enhance fiber–matrix adhesion by increasing surface roughness and introducing oxygen-containing functional groups, leading to notable improvements in tensile strength and fracture toughness, as well as shifts in the dominant failure mechanisms [7]. Collectively, these approaches highlight that optimizing interfacial interactions and microstructural design is critical for controlling damage initiation and propagation in CFRP laminates.

Acoustic emission (AE) has been evaluated in CFRP under Mode-I loading, demonstrating that AE signals can effectively monitor delamination onset and progression. The study employs wavelet analysis to correlate AE frequency content with damage evolution, providing valuable insights into the fracture process [8–10]. Another study

* Corresponding author at: Mechanical and Industrial Engineering Department, Universitas Gadjah Mada (UGM), Indonesia.
E-mail address: akhsin.muflikhun@ugm.ac.id (M.A. Muflikhun).

https://doi.org/10.1016/j.rineng.2026.110850
Received 17 March 2026; Received in revised form 30 April 2026; Accepted 2 May 2026
Available online 2 May 2026

enhances CFRP composites by improving toughness, impact resistance, and defect detection. MWCNT-doped PES films boost electrical conductivity and fracture toughness [11], while MWCNTs and CSR particles synergistically increase toughness by 149 % (Mode I) and 80 % (Mode II), improving impact resistance [12]. Advanced NDT techniques refine defect visualization for better structural assessment [13].

Further investigations into Mode-II fracture behaviour of CFRP laminates reveal complex micromechanical failure mechanisms, including plastic deformation, fiber/matrix debonding, and microcrack formation [14–16]. High-resolution in situ optical and X-ray computed tomography (CT) imaging capture progressive damage, enabling precise correlations between microscopic failure and macroscopic fracture toughness [14,17]. Building on this, recent research integrates acoustic emission (AE) with Digital Image Correlation (DIC) to classify CFRP damage mechanisms under different loading conditions using machine learning techniques. By combining AE clustering with DIC strain analysis, this study effectively distinguishes intra- and inter-laminar damage modes, aiding structural health monitoring and predictive damage modeling [18]. Recent advances in AE signal processing further highlight AE's capability for damage classification in composite structures through signal decomposition and time–frequency analysis. However, challenges remain in separating overlapping multi-mode damage signals [19].

Recent studies of ultrasonic-based techniques, particularly guided Lamb waves, have demonstrated strong potential for detecting delamination and internal defects in composite laminates due to their high sensitivity and large-area inspection capability. However, their effectiveness can be affected by signal dispersion and mode complexity [20]. Comprehensive reviews on ultrasonic NDT methods also emphasize their reliability and widespread application in composite structures, while highlighting key limitations such as anisotropy effects and difficulties in subsurface defect characterization [21]. Beyond Mode-II fracture, studies have also explored the broader mechanical behaviour, damage mechanisms, and degradation of CFRP composites under various conditions. For instance, one investigation examines Mode-I and Mode-II fracture toughness using multi-instrument structural health monitoring methods, integrating AE and infrared thermography (IRT) to classify failure types such as fiber breakage and matrix cracking. The findings suggest that twill-woven laminates are more prone to delamination failures than other configurations [22,23].

Furthermore, recent studies have demonstrated that AE-based monitoring can effectively identify fracture mechanisms and capture the influence of stacking sequence on damage evolution in composite laminates, providing deeper insight into the relationship between AE signal characteristics and physical failure processes [24]. In parallel, a semi-analytical model has been developed to predict Mode-II fracture toughness in multidirectional laminates, demonstrating that interfacial angles and intra-ply damage strongly influence fracture energy. Experimental validation confirms the model's predictive accuracy, highlighting its potential for structural design optimization [25]. Damage detection techniques have also been a focus of research, particularly in the context of CFRP-strengthened concrete structures. A review of non-destructive testing (NDT) methods underscores the importance of advanced techniques such as ground-penetrating radar and impact-echo testing for assessing delamination, debonding, and overall structural integrity [26]. Furthermore, a study on the thermal aging degradation of CFRP composites highlights reductions in mechanical properties, with Young's modulus decreasing by 21 % and strength by 34 % after prolonged high-temperature exposure, indicating the need to assess thermal resistance for long-term applications [27].

Numerous studies have explored various aspects of CFRP and GFRP composites, including fracture mechanics, fatigue behaviour, damage detection, and structural applications [28]. Research on fatigue crack growth in composite-to-steel bonded interfaces using ENF highlights the importance of shear-strain-based monitoring and numerical modeling for predicting crack propagation [29]. Additionally, the influence of geometric and material parameters on Mode-II fatigue behavior has been investigated using cohesive zone modeling, revealing key factors that affect delamination resistance [30]. Advancements in non-destructive testing (NDT) methods have significantly contributed to damage detection in CFRP composites. Electromagnetic wave-based NDT (EMW-NDT) has been proposed for identifying delaminations and cracks via electromagnetic interference shielding [31]. Similarly, high-speed eddy current testing (ECT) has been successfully applied to detect delaminations with rapid, accurate results [32–34]. Thermal NDT techniques, coupled with neural networks, have also demonstrated high precision in characterizing defect depth, enhancing the reliability of hidden defect detection in CFRP structures [35].

Efforts to enhance CFRP's mechanical performance have led to innovative material designs. A bio-inspired CFRP laminate, mimicking nacre's "brick-and-mortar" structure, exhibits significant improvements in interlaminar and translaminar fracture toughness [36]. Additionally, hybrid CFRP composites reinforced with graphene oxide and carbon nanotubes show substantial toughness enhancements under Mode-I and Mode-II fracture tests [37]. Investigations into the effects of low-temperature exposure on CFRP-steel hybrid laminates emphasize the importance of accounting for thermal residual stresses in fracture mechanics [38]. Beyond material improvements, CFRP's role in structural applications has been widely explored. Studies on CFRP-strengthened steel beams show that laminates with end-chorage plates significantly enhance flexural strength while reducing deflection [39,40]. Moreover, a systematic failure analysis of fractured CFRP specimens subjected to various mechanical tests highlights the effectiveness of SEM and optical microscopy in understanding fracture behavior under different loading conditions [41]. Further research focuses on mechanical properties, damage mechanisms, and structural health monitoring (SHM) using experimental and numerical approaches. Crack propagation in adhesively bonded CFRP joints has been analyzed using high-resolution optical fiber sensing during ENF and DCB tests, thereby improving the accuracy of fracture toughness assessment [42,43]. Finite element modelling of interlaminar delamination confirms that fiber orientation significantly influences fracture toughness, emphasizing the role of ply angle in laminate performance [44].

In situ microscopic observations of CFRP adhesive joints under Mode-I and Mode-II loading provide deeper insights into strain concentration and crack growth behaviours [45]. Studies on Mode-II interlaminar fracture toughness in GFRP laminates using ENF tests validate the effectiveness of the cohesive-zone method for delamination modelling [46]. Meanwhile, interleaving CFRP laminates with PA66 electrospun nanofibers has been shown to enhance fracture toughness by mitigating fiber breakage and matrix cracking [47]. Recent investigations also explore the influence of stacking sequences and curvature on fracture behaviour. Asymmetrical stacking sequences in filament-wound CFRP specimens exhibit distinct delamination patterns under DCB, ENF, and MMB tests [48]. Similarly, ENF testing of curved CFRP beams provides validated data reduction methods for Mode-II fracture toughness evaluation [49]. Advances in damage detection techniques continue to improve SHM strategies. A novel electromagnetic NDT method based on power loss effectively detects cracks and fiber distribution in CFRP laminates [50]. A comprehensive review of SHM techniques that add natural fiber reinforcement to polymer joints categorizes intrinsic and extrinsic sensing methods and emphasizes their applications in real-world structures [51,52]. Lastly, a waveform-based clustering and machine learning approach integrates acoustic emission data for real-time damage classification, enhancing predictive capabilities for CFRP component failures [53].

The basic evaluation previously introduced by researchers to evaluate CFRP laminates often did not include NDT methods, especially AE and ultrasound analysis, for Mode II (GIIC) fracture toughness. Only a few studies reported by compiling several papers and discussing them in a review style [54–56]. Moreover, the combination of NDT and theoretical analysis with residual stress correction has not been reported

previously, especially in terms of Mode II with CFRP laminates. Despite extensive investigations on CFRP laminates, a comprehensive understanding of Mode II damage evolution in thin laminates using integrated NDT approaches remains limited, particularly in correlating real-time signals with fracture mechanisms. The novelty of this study lies in integrating AE and ULW monitoring with theoretical fracture analysis and stress considerations within a unified experimental framework, specifically applied to Mode II fracture behavior of thin CFRP laminates. Therefore, this study aims to systematically investigate the influence of stacking sequence on the interlaminar fracture behaviour of thin CFRP laminates under ENF loading, incorporating AE and ULW. The primary objective is to quantify the damage initiation, propagation, and energy-release characteristics using a combination of acoustic emission and ULW techniques. Secondary objectives include establishing direct correlations between NDT signal features (energy, duration, and frequency) and underlying damage mechanisms, and validating these findings using destructive characterization methods, such as SEM and Shore D hardness measurements. Furthermore, this work introduces a unified experimental framework that integrates real-time monitoring with post-mortem validation to enhance the reliability of damage interpretation in composite laminates. The study further provides a comparative assessment of stacking-sequence-dependent damage evolution, highlighting the role of ply orientation in governing delamination resistance and crack propagation stability. The outcomes of this research offer valuable insights for developing robust structural health monitoring strategies for advanced thin composite structures, particularly in aerospace and space applications where inspection accessibility is limited and early damage detection is critical.

2. Materials and methods

2.1. Laminates materials and manufacturing

In this study, a unidirectional carbon fiber prepreg from Hexcel, specifically HexPly M21/34 %/UD194/T800S–24K/600HLU, was utilized. This prepreg consists of a 34 % resin matrix reinforced with 194 gsm unidirectional T800S-24 K fibers. The detailed material properties of the prepreg are presented in Table 1. The composite laminates were fabricated using the autoclave method, following two different stacking sequences: $[+45°/-45°/0°]_{2S}$ and $[0°/+45°/-45°]_{2S}$. These sequences correspond to the layer arrangements of $[+45°/-45°/0°/0°/-45°/+45°/+45°/-45°/0°/0°/-45°/+45°]$ and $[0°/+45°/-45°/-45°/+45°/0°/0°/+45°/-45°/-45°/+45°/0°]$, respectively. The autoclave curing process was carried out at 180 °C for 4 h under 7 Bar, while the ambient temperature remained at 25 °C. The samples were precisely cut using an ATM Brillant 220 machine in accordance with ASTM D-7905. Mechanical testing was conducted to evaluate the material properties. Tensile tests revealed that the laminate with the $[0°/+45°/-45°]_{2S}$ layup exhibited an elastic modulus of 61.49 GPa, while the $[+45°/-45°/0°]_{2S}$ configuration demonstrated a slightly lower modulus of 60.47 GPa. In terms of ultimate tensile strength, the $[0°/+45°/-45°]_{2S}$ laminate achieved 1123.97 MPa, whereas the $[+45°/-45°/0°]_{2S}$ laminate performed slightly better, reaching 1227.95 MPa. Fig. 1(a) showed the manufacturing process, Fig. 1(b) showed the ENF test setup, and the sample after the test was shown in Fig. 1(c). A total of 8 samples were tested, 4 from each combination. The details of all specimens tested in the present study are shown in Table 2.

Specimens were manufactured and cut according to ASTM D-7905, as shown in Fig. 2(a), where 2b is the width of the specimen, l is the total sample length. The stacking sequences of the samples are illustrated in Fig. 2(b). The side part of the specimen was marked using spray paint, while the black markings were made with a sharp pencil at specified distances in accordance with the standard of ASTM D-7905. Detailed information on the dimensions of the specimen and the laminate sequences can be seen in Table 1. The detailed sample setup during the ENF test is shown in Fig. 3, based on the ASTM D-7905 schematic. It is shown that 2 h is total thickness, r_1 is the radius of upper indenter, r_2 is the radius of lower indenter, a is the crack length, a_I is the length between crack tip and the edge of sample (30 mm), L is distance of half upper and lower indenter (50 mm), c is the distance of the sample edge with the center of lower indenter, and L_u is the distance of the sample end edge with the center of lower indenter. The present

Table 1
The Properties of materials used in the present study [57–60].

	Properties	Value	Units
Manufacturing Process Parameter	Autoclave temperature	180	°C
	Autoclave time	4	h
	Autoclave press.	7	bar
	Fiber volume fraction	59.2	%
	Prepreg mass (cured)	294	g/m^2
	Glass Transition Temp.	195	°C
Mechanical Properties	UTS (ASTM D3039)	2860	MPa
	Tension Modulus (ASTM D3039)	160	GPa
	Longitudinal modulus (E_1)	130.7	GPa
	Transverse modulus (E_2)	8.01	GPa
	ILSS (ASTM D2344)	110	MPa
	Transverse tensile strength (Y^T)	40.5	MPa
	Shear strength (S^L)	69.6	MPa
	Compression Strength (ASTM D695)	1790	MPa
	Compression Modulus (ASTM D695)	148	GPa
	Poisson's ratio (ϵ_{12})	0.35	-
	Shear modulus (G_{12})	5.31	GPa
Thermal Properties	Longitudinal CTE α	−5.02E-07	$°C^{-1}$
	Transverse CTE α	6.10E-06	$°C^{-1}$

2.2. AE and ULW evaluation

NDT evaluation was additionally performed in this study following specimen failure. Ultrasonic inspection was conducted using a USPC 3040 DAC system (Ingenieurbüro, Hillger NDT GmbH, Germany) operating in an immersion-based pulse–echo configuration. The measurements were carried out in a deionized water bath, with both the ultrasonic probe and the specimen fully immersed to ensure stable, consistent acoustic coupling. A piezoelectric ultrasonic transducer, acting as both transmitter and receiver, was employed to generate and detect longitudinal ultrasonic waves. The excitation was provided by a short electrical pulse, producing high-frequency acoustic waves that propagate through the laminate and reflect at material interfaces and internal discontinuities.

A calibrated acoustic velocity, corrected for specimen thickness, was used to accurately interpret time-of-flight signals. The inspection was performed using an automated raster-scanning approach in the x–y direction, providing full-area coverage of the specimen surface. Gate settings were defined within the acquisition software to isolate entry signals, internal defect reflections, and backwall echoes, allowing depth-resolved analysis of the laminate structure. The resulting C-scan images map variations in signal amplitude and time-of-flight across the plate, providing an indirect assessment of thickness variations and fiber distribution. In addition, these images enable identification of regions with defect concentration, such as delamination zones and fiber agglomeration, based on localized changes in ultrasonic response.

AE monitoring was conducted using a Micro-II Digital AE System (Physical Acoustics Corporation, Mistras, NJ, USA). Wideband differential AE sensors (WD type, frequency range 100–900 kHz) were employed, coupled with a 40 dB preamplifier. Data acquisition was performed at a sampling rate of 5 MSPS with a pre-trigger length of 256 samples. A 20 kHz analog high-pass filter was applied to reduce low-frequency noise. The AE signal timing parameters were defined as

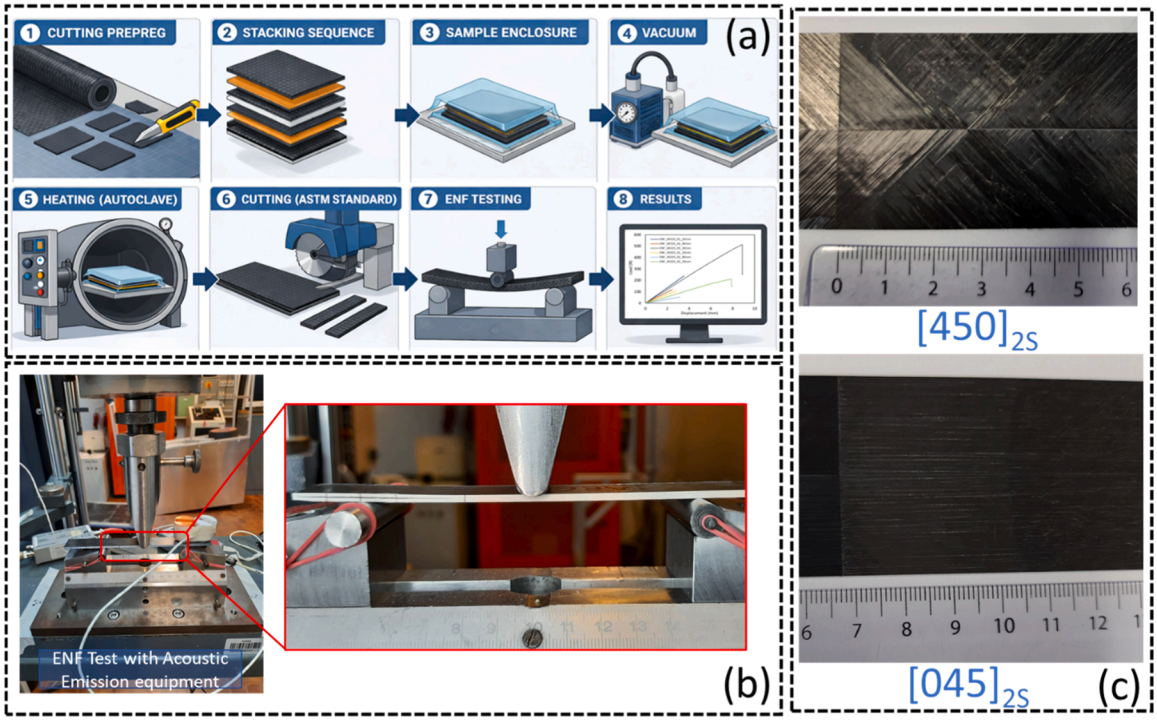

Fig. 1. (a) Schematic study, (b) ENF testing condition, (c) Sample after testing.

Table 2
The specimen dimension.

Sample	*l (mm)*	*2b (mm)*	*2 h (mm)*	*al (mm)*	*C (mm)*	*lu (mm)*
0452S 01	288	19.82	2.25	68	38	146.5
0452S 02	288	20.51	2.29	68	38	146.5
0452S 03	288	20.40	2.29	68	38	146.5
0452S 04	288	20.10	2.29	68	38	146.5
4502S 01	292	20.38	2.26	71.5	41.5	150.5
4502S 02	292	20.55	2.28	71.5	41.5	150.5
4502S 03	292	20.34	2.22	71.5	41.5	150.5
4502S 04	292	20.12	2.27	71.5	41.5	150.5

follows: Peak Definition Time (PDT) = 50 μs, Hit Definition Time (HDT) = 200 μs, and Hit Lockout Time (HLT) = 300 μs. The detection threshold was set to approximately 45–50 dB, based on the measured background noise level, to ensure reliable discrimination of valid AE events.

Sensor placement was defined according to the ENF test configuration shown in Fig. 1(b), with sensors positioned near the load introduction and support regions to enhance sensitivity to interlaminar damage and crack-propagation events. In this study, AE analysis focuses on global signal trends (e.g., cumulative hits, energy, duration, and frequency evolution) to characterize damage progression. Advanced clustering or feature-based classification techniques were intentionally not employed, as the objective is to establish a direct correlation between AE activity and macroscopic damage evolution rather than to perform discrete damage mode separation. This approach avoids overinterpretation of overlapping AE signatures and is consistent with the scope of the present experimental framework. Each specimen was evaluated using both AE and ultrasonic methods, and the measurement settings were defined according to the standard operating procedures of the respective systems. To avoid overinterpretation of AE signals, damage mechanisms in this study are not directly classified using clustering or machine learning techniques. Instead, AE parameters are interpreted in conjunction with macroscopic observations (crack propagation), surface roughness analysis, and SEM fracture morphology.

2.3. Fracture toughness Mode II calculations

The basic calculation of interlaminar fracture toughness in mode II using NPC (Non-Pre-crack) initiation value of GIIC is determined from the maximum force (P_{Max}). The *C* as compliance can be determined in Eq. (1).

$$C = A + ma^3 \tag{1}$$

Where A is the intercept and m is the slope obtained from regression analysis. Here, the G_{IIC} can be determined by using Eq. (2).

$$G_{IIC} = \frac{3mP_{MAX}^2 a^2}{4b} \tag{2}$$

Where m is the CC coefficient, P_{MAX} is the maximum force, *a* is the crack length, and *2b* is the specimen width.

For the series of tests, the average of the G_{IIC} can be further analyzed using the statistical method described in ASTM D7905, using Eqs. (3), 4, and 5.

$$\overline{x} = \frac{1}{n}\sum_{i=1}^{n} x_i \tag{3}$$

$$S_{n-1} = \sqrt{\frac{\sum_{i=1}^{n} x_i^2 - n\overline{x}^2}{n-1}} \tag{4}$$

$$CV = 100\ x\ \frac{S_{n-1}}{\overline{x}} \tag{5}$$

Where: $\overline{x}$ is the sample mean (average), S_{n-1} is the sample standard deviation, *CV* is the coefficient of variation (%), *n* is the number of specimens, and x_i is a measured or derived value.

3. Results and discussion

3.1. ENF Test

The load-displacement relationship for ENF is shown in Fig. 4. The

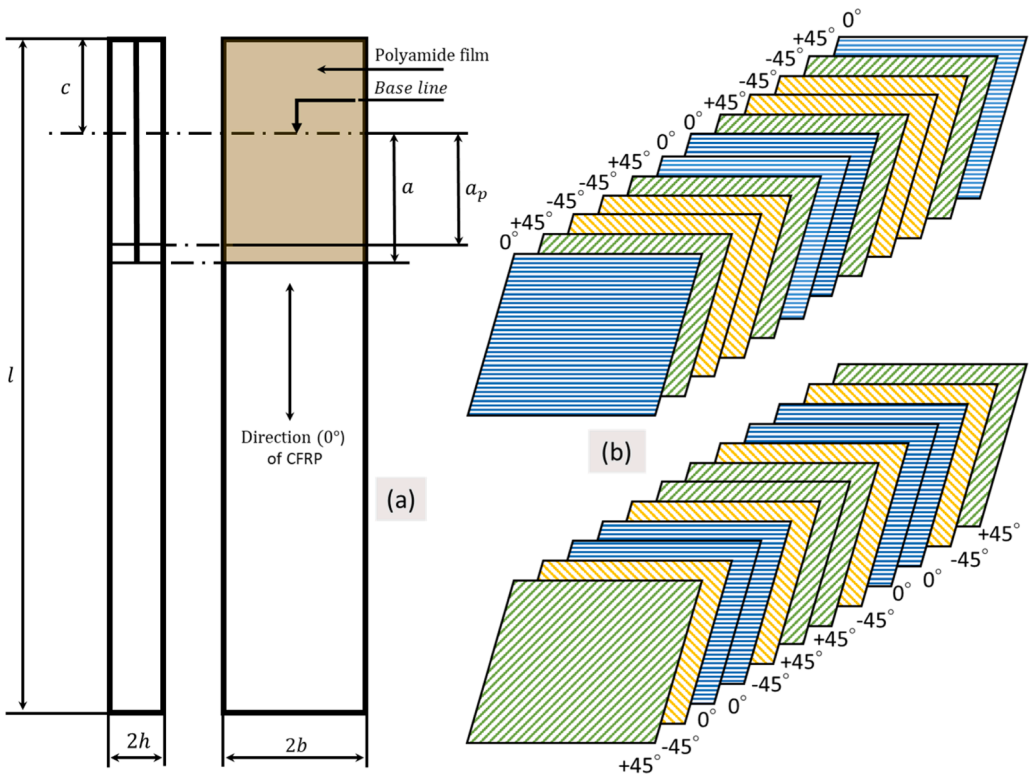

Fig. 2. (a) ENF Sample dimension, (b) Sample stacking sequences.

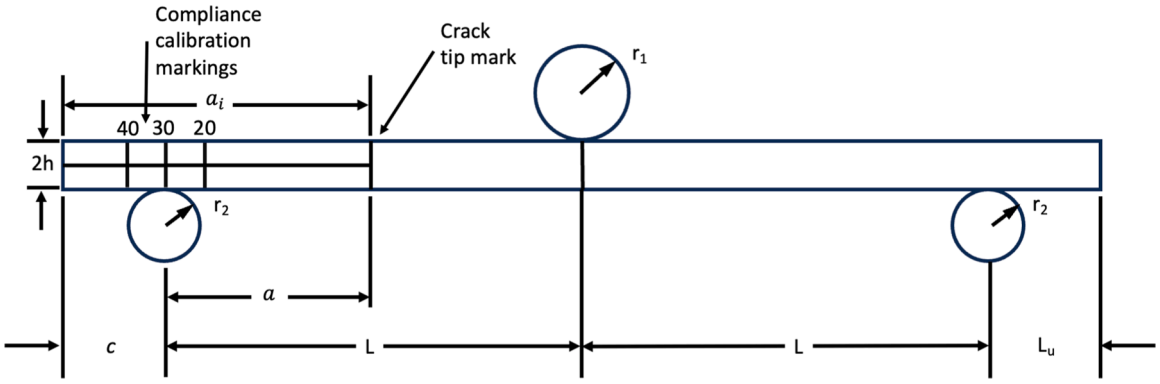

Fig. 3. Schematic Testing of ENF.

full series of tested samples is illustrated in Fig. 4(a). It is shown that the [0°/+45°/−45°]2S layup has a higher load than the [+45°/−45°/0°]2S layup, by >2x. For the ENF 3 model loaded with the dedicated distance based on the NPC (Non-Pre Crack) model, the results are shown in Fig. 4 (b). It is shown that from 20 mm, 40 mm, and 30 mm distances, the $[0°/+45°/-45°]_{2S}$ layup surpasses the $[+45°/-45°/0°]_{2S}$ layup for all combinations. These results show that the sequences and thicknesses of the laminates play crucial roles in composite laminates. It is also indicated that thicker laminates reveal more predefects. This trend is shown in the 0° layer of both laminates ($[0°/+45°/-45°]_{2S}$ layup and $[+45°/-45°/0°]_{2S}$ layup).

An additional observation from Fig. 4(a) concerns the laminate's stiffness behavior. It is indicated by the slope of the load–displacement curves. The specimens with the $[0°/+45°/-45°]_{2S}$ layup show a steeper initial slope compared with the $[+45°/-45°/0°]_{2S}$ layup, indicating a higher flexural stiffness during the initial loading stage. This behavior is associated with the presence of 0° plies near the outer layers, which significantly contribute to resisting bending loads and delaying crack propagation during the ENF test. Consequently, the laminates with this configuration can sustain higher loads before a sudden drop, indicating the onset of delamination or crack growth. In contrast, the $[+45°/-45°/0°]_{2S}$ layup laminates exhibit lower stiffness and earlier load drops, suggesting that the ply orientation sequence influences not only the maximum load capacity but also the stability of crack propagation during loading.

Fig. 5 presents the relationship between compliance (C) and crack length (a) used for determining the Mode II interlaminar fracture toughness (G_{IIc}) of the CFRP laminates during the ENF test. The plots show a linear increase in compliance with increasing crack length for both stacking sequences, which confirms the validity of the compliance calibration method used for G_{IIc}evaluation. For the $[0°/+45°/-45°]_{2S}$ laminates (Fig. 5 lower), the compliance values increase gradually from approximately 0.015–0.016 mm/N at $a = 20$mm to about 0.021–0.022 mm/N at $a = 40$mm, indicating a moderate increase in structural flexibility as the crack propagates. The fitted linear relations for each specimen show slopes around 0.0029, suggesting relatively consistent

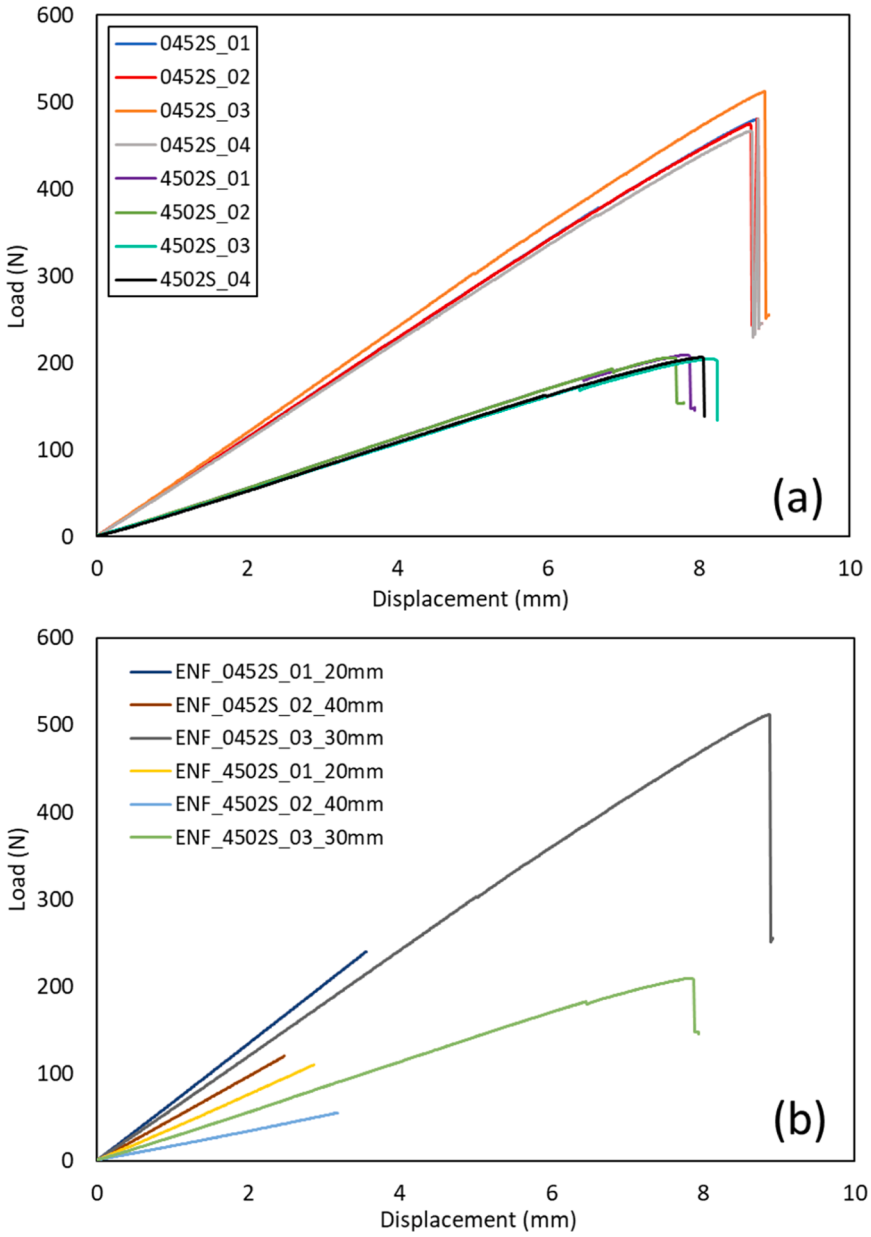

Fig. 4. (a) Final load of all samples, (b) Representative sample of 2 combinations.

crack-growth behavior across the samples. The trend is shifted when the $[+45°/-45°/0°]_{2S}$ laminate (Fig. 5 upper) exhibits higher compliance values overall, increasing from approximately 0.016–0.027 mm/N at a = 20mm to nearly 0.059–0.061 mm/N at a = 40mm.

The linear-fitting slopes range from 0.016 to 0.017, which are significantly higher than those of the $[0°/+45°/-45°]_{2S}$ laminate. This indicates that the $[+45°/-45°/0°]_{2S}$ laminate experiences a faster increase in flexibility as the crack length grows, reflecting lower resistance to interlaminar crack propagation. The higher compliance and steeper slopes suggest that the stacking sequence strongly influences the structural stiffness and fracture response of the laminates during Mode II loading.

Fig. 6 presents the Mode II interlaminar fracture toughness (G_{IIc}) obtained from the ENF tests for the two laminate stacking sequences. For the $[0°/+45°/-45°]_{2S}$ layups (Fig. 5(a)), the measured G_{IIc} values range between approximately 1.52 kJ/m^2 and 1.89 kJ/m^2, with the average value recorded at 1.7 kJ/m^2, indicating a phenomenon of interlaminar shear crack propagation. For the $[+45°/-45°/0°]_{2S}$ layup, the G_{IIc} values are around 1.69 kJ/m^2 to 1.82 kJ/m^2 with the average is 1.78 kJ/m^2, which remain higher compared with $[0°/+45°/-45°]_{2S}$ layups.

The overall fracture toughness of this laminate is slightly lower and shows a narrower distribution. This difference indicates that the stacking sequence plays a critical role in governing the interlaminar fracture behavior under Mode II loading. The slightly higher G_{IIc} observed in the $[+45°/-45°/0°]_{2S}$ laminates can be attributed to the presence of ±45° plies near the outer layers, which promote crack deflection, fiber–matrix debonding, and local fiber bridging. These mechanisms increase energy dissipation during crack propagation, leading to a more stable and progressive delamination process. In contrast, the $[0°/+45°/-45°]_{2S}$ laminates tend to exhibit a more direct crack path along the interface, leading to lower resistance to crack growth and more unstable propagation behavior.

Further statistical analysis was performed in accordance with ASTM D7905 to evaluate the reliability of the obtained results (Based on Eq (3)–5). The $[0°/+45°/-45°]_{2S}$ laminates show an average G_{IIc} of 1.70 kJ/m^2 with a standard deviation of 0.16 kJ/m^2 and a coefficient of variation (CV) of 9.49 %, indicating a relatively higher data scatter. Meanwhile, the $[+45°/-45°/0°]_{2S}$ laminates exhibit an average G_{IIc} of

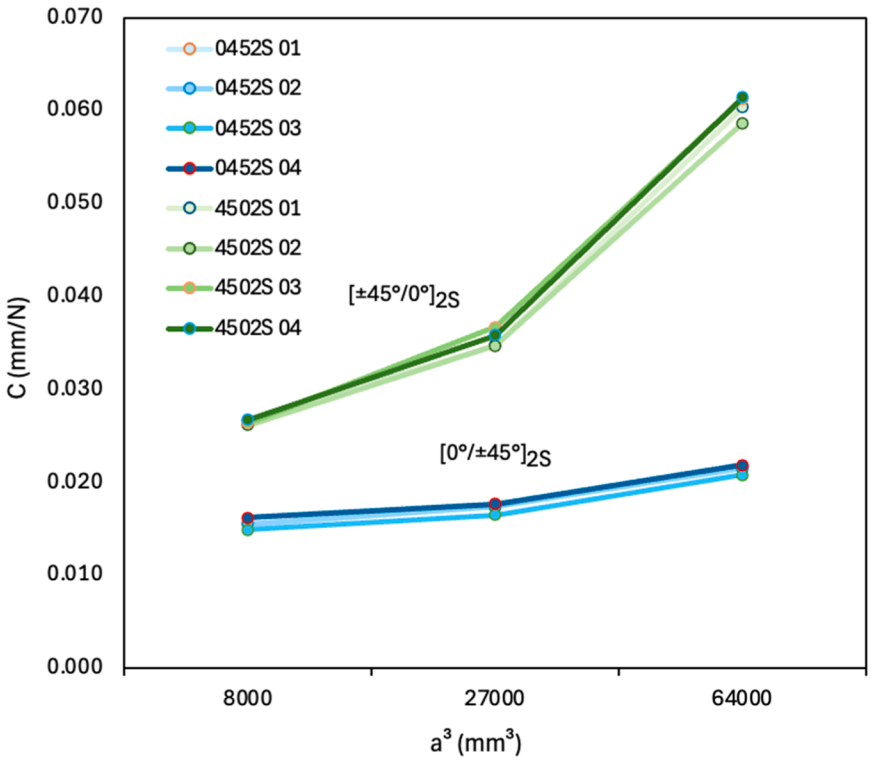

Fig. 5. C vs a^3 in GIIc of the study. $[0°/+45°/-45°]_{2S}$ layups (Lower), $[+45°/-45°/0°]_{2S}$ layups (Upper).

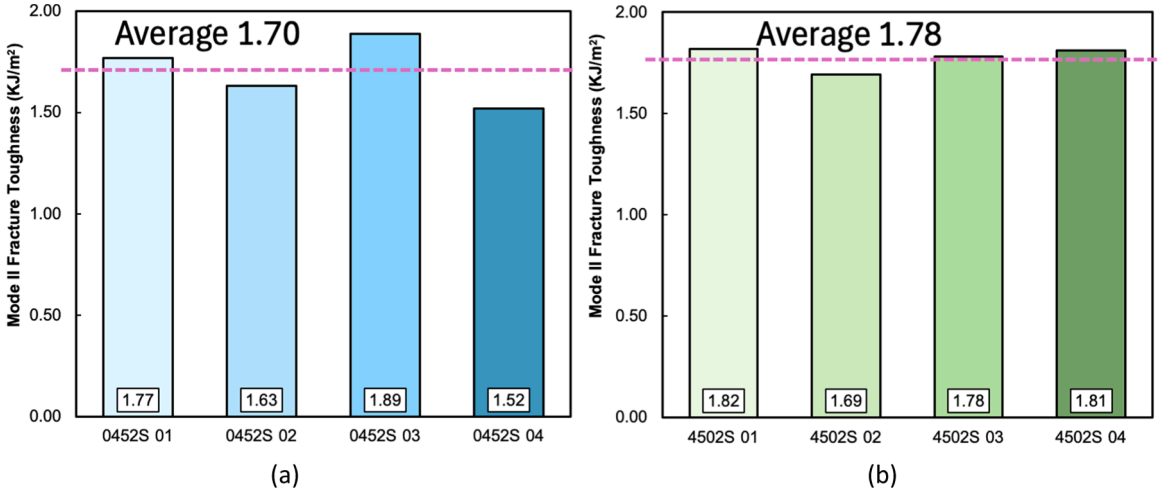

Fig. 6. G_{IIc} of the study. (a) $[0°/+45°/-45°]_{2S}$ layup, (b) $[+45°/-45°/0°]_{2S}$ layup.

1.78 kJ/m^2 with a lower standard deviation of 0.06 kJ/m^2 and a CV of 3.33 %, reflecting more consistent and repeatable behavior. These statistical results confirm that although the difference in mean fracture toughness is relatively small, the $[+45°/-45°/0°]_{2S}$ configuration provides more stable and reliable fracture performance under Mode II loading.

Time-to-time analysis of the specimen $[0°/+45°/-45°]_{2S}$ layup is shown in Fig. 7. It is shown that the laminates can withstand without any visual crack detected until the final catastrophic crack. From the beginning of the test until approximately 17:54, the laminate exhibits gradual flexural deformation without any visible crack initiation along the mid-plane interface. The specimen continues to bend under increasing load while maintaining structural integrity, indicating that the laminate stacking sequence can sustain significant deformation before damage onset.

A more detailed observation between 17:54 and 17:55 reveals the sudden onset of crack propagation. Just before the crack occurs (17:54), the laminate still appears intact with only noticeable bending deformation beneath the loading nose. However, within one second (17:55), a clear interlaminar crack rapidly propagates along the interface region, as highlighted in Fig. 7. This abrupt transition from a visually intact condition to catastrophic crack growth indicates a brittle-like delamination event typical in interlaminar fracture under ENF loading. The crack propagation occurs almost instantaneously once the critical strain energy release rate is reached, confirming that the laminate stores elastic energy during deformation and releases it suddenly at the moment of failure.

The step-by-step crack propagation during the ENF test of the $[+45°/-45°/0°]_{2S}$ layup is shown in Fig. 8. The sequential images show the deformation process as the loading progresses, where the numbers

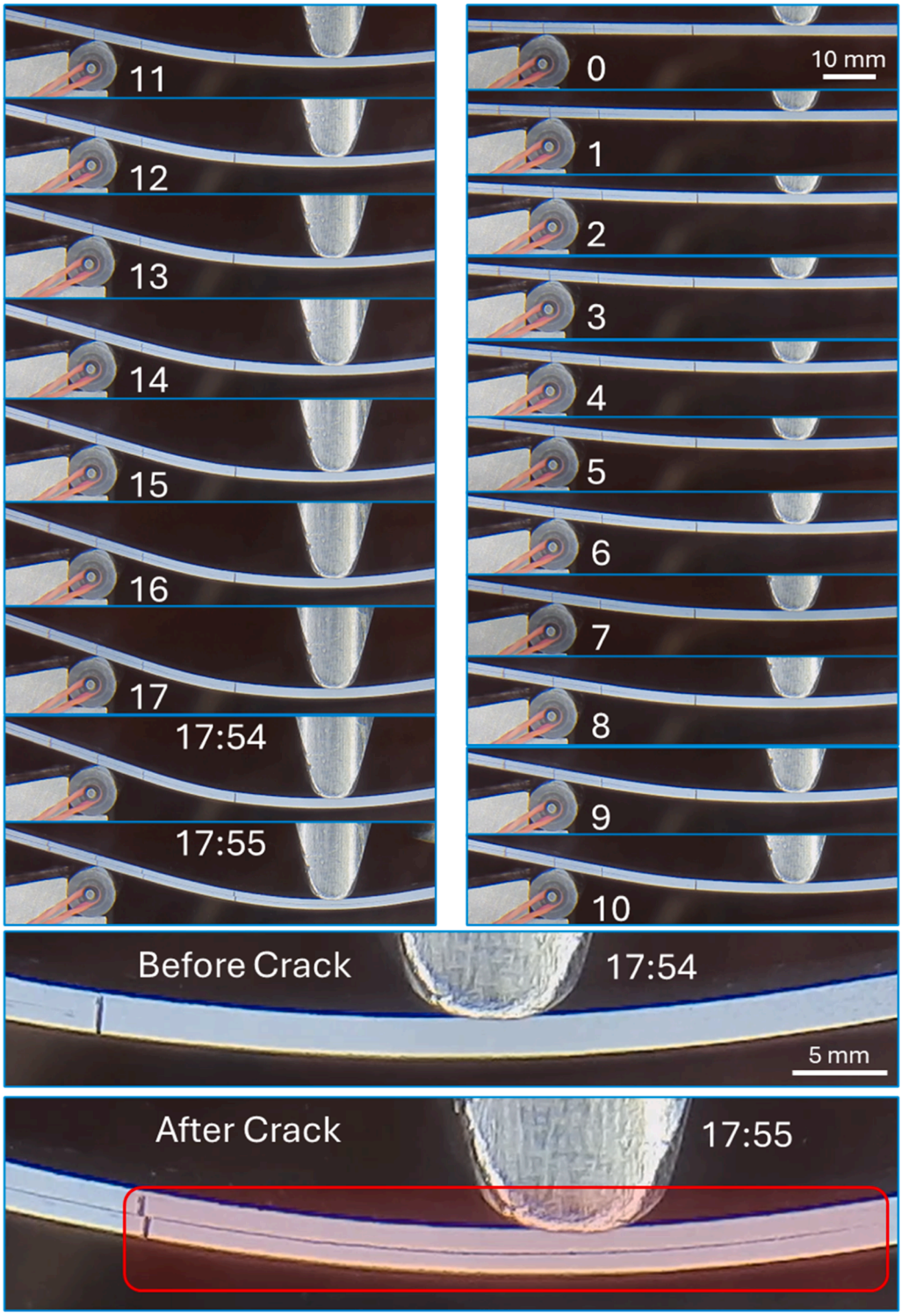

Fig. 7. Crack propagation of $[0°/+45°/-45°]_{2S}$ layup. Number is in Min.:Sec.

represent the testing time in minutes and seconds. Unlike the $[0°/+45°/-45°]_{2S}$ layup, which maintained structural integrity until a sudden catastrophic crack occurred, the $[+45°/-45°/0°]_{2S}$ layup configuration shows an earlier indication of crack initiation. The first visible crack appears around minute 13, suggesting that the interlaminar (debonding between 45° layers) region begins to experience localized damage earlier in the loading process. The presence of ±45° plies near the outer layer likely influences the stress distribution and shear deformation, which contributes to the earlier onset of crack initiation. As the loading continues, the crack propagates gradually along the mid-plane interface, as highlighted in the red-marked regions between 16:05 and 16:40. The images clearly demonstrate that the crack length increases progressively with increasing displacement and bending deformation. This progressive crack growth indicates a more stable delamination propagation compared with the sudden failure observed in the previous layup configuration. The laminate undergoes continuous energy release during crack extension, allowing the crack to propagate step by step rather than occurring instantaneously. Such behavior suggests that the stacking

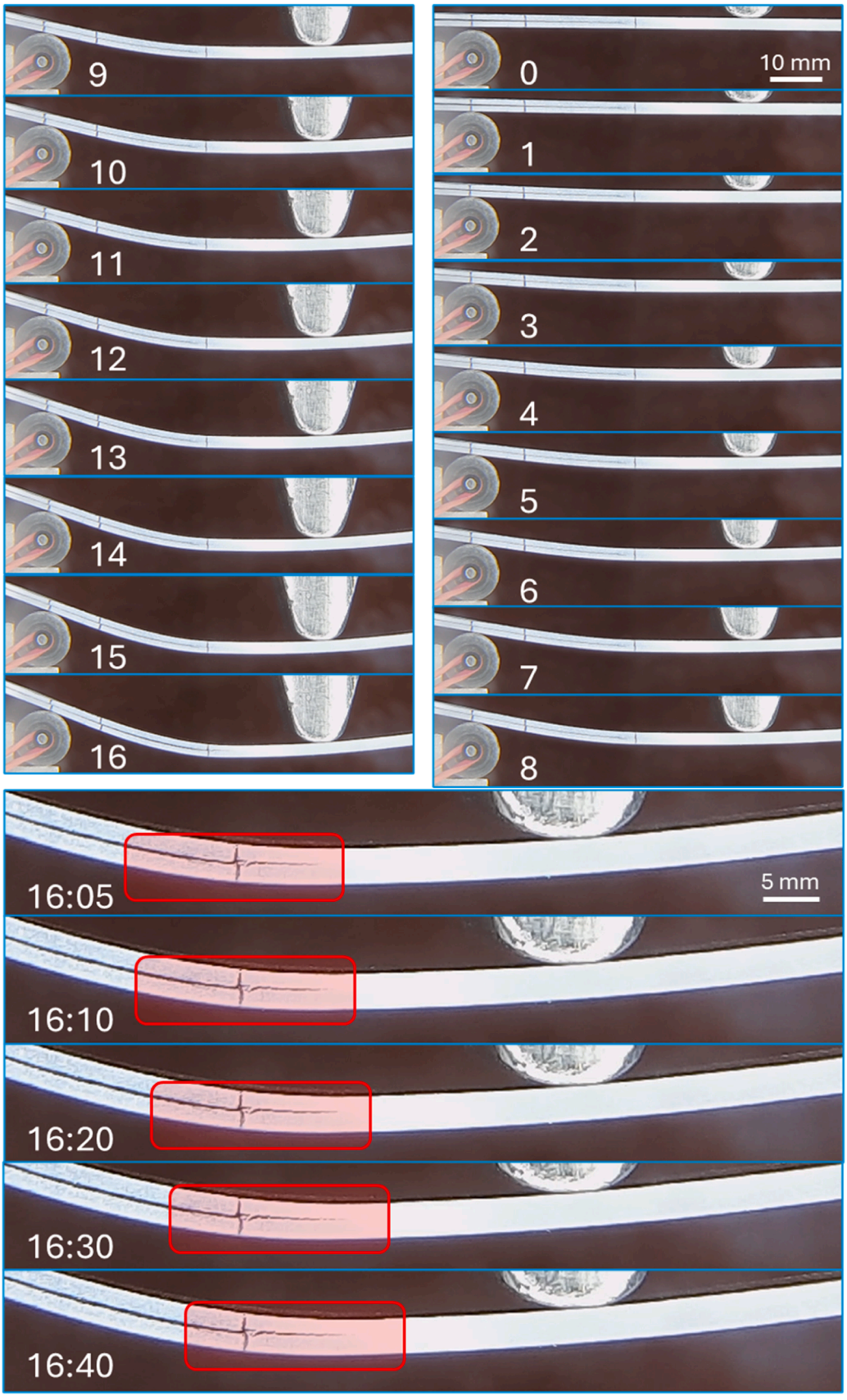

Fig. 8. Crack propagation of $[+45°/-45°/0°]_{2S}$ layup. Number is in Min.:Sec.

sequence significantly affects the fracture mechanism and the laminates' energy-dissipation capability, with the $[+45°/-45°/0°]_{2S}$ layup exhibiting a more gradual crack-propagation pattern before reaching final failure.

3.2. Roughness

Roughness evaluation of the delaminated layer after the ENF test is illustrated in Fig. 9 for the [0°/+45°/−45°]2S layup and in Fig. 10 for the $[+45°/-45°/0°]_{2S}$ layup. Since the layer interface was different, the 0° layers after delamination formed a straight crack perpendicular to the crack growth. The optical observation shows that the delaminated interface is relatively smooth and aligned with the fiber orientation, particularly in the region where the 0°ply is exposed, which is clearly shown in Fig. 9. The crack propagation direction is perpendicular to the 0° direction. The fracture surface appears straighter, with limited fiber bridging or pull-out features in fiber-oriented samples. This condition indicates that the crack propagated primarily along the matrix-dominated interface, producing a relatively uniform delamination surface. The quantitative roughness profile extracted from the marked regions in Fig. 9 further confirms this observation. The surface profile shows gradual height variations along the measured line, indicating moderate surface irregularity.

The measured roughness parameters reveal that the delaminated interface exhibits relatively lower roughness values with Ra = 8–12 μm, and Rz = 37–44 μm. This suggests that the crack propagated in a more brittle, direct manner, with limited resistance from the fiber orientation. This behavior is consistent with the previously observed sudden catastrophic crack, in which the stored elastic energy was released rapidly once the critical fracture condition was reached.

In the other laminates, the roughness characteristics of the $[+45°/-45°/0°]_{2S}$ layup shown in Fig. 10 exhibit a more complex surface morphology. The fracture surface displays more pronounced texture and waviness due to the presence of ±45° fiber orientations near the delamination interface. These angled fiber layers introduce additional shear interaction and crack deflection during propagation, resulting in a rougher delaminated surface. The corresponding roughness profiles show larger amplitude variations along the measurement path with Ra and Rz equal to 25–31 μm and 90–100 μm, respectively. This indicates increased surface irregularities. This suggests that the crack propagation experienced greater resistance and dissipated more energy through mechanisms such as fiber-matrix debonding, fiber bridging, and crack path deviation.

The surface profile of the $[0°/+45°/-45°]_{2S}$ laminates shows a smoother, more gradual trend, with the roughness curve increasing steadily over the measured length. This indicates a relatively uniform fracture surface with limited height variation, consistent with crack propagation along the interface dominated by the 0°ply orientation with the delaminated surface appears more continuous and stable. On the other hand, the $[+45°/-45°/0°]_{2S}$ laminates exhibit a pronounced up–down roughness profile with clear peaks and valleys. This irregular morphology is attributed to the ±45° fiber orientations near the delamination interface, which induce crack deflection and additional resistance during propagation, resulting in a rougher fracture surface.

3.3. Acoustic emission (AE) test

Fig. 11 presents the AE response of the $[0°/+45°/-45°]_{2S}$ laminate under ENF testing with different loading lengths of 20 mm, 30 mm, and 40 mm. The left plots illustrate the cumulative AE hits as a function of time, while the right plots show the amplitude distribution of the detected AE signals. For the 20 mm loading condition, only a small number of AE hits are detected, and the cumulative curve shows a minimal step increase. This indicates that only limited microdamage occurred during loading.

The corresponding amplitude distribution also shows only a few scattered signals, suggesting that the laminate remained relatively stable, with no significant crack propagation. For the 40 mm loading condition, the cumulative AE hits increase gradually as loading progresses. Several step-like increments appear in the cumulative hit curve, indicating intermittent micro-damage events such as matrix cracking or minor interfacial debonding within the laminate. The amplitude distribution shows a moderate number of AE events with amplitudes distributed around the mid-range values.

This behavior suggests that the laminate begins to accumulate internal damage before reaching the final fracture stage, indicating

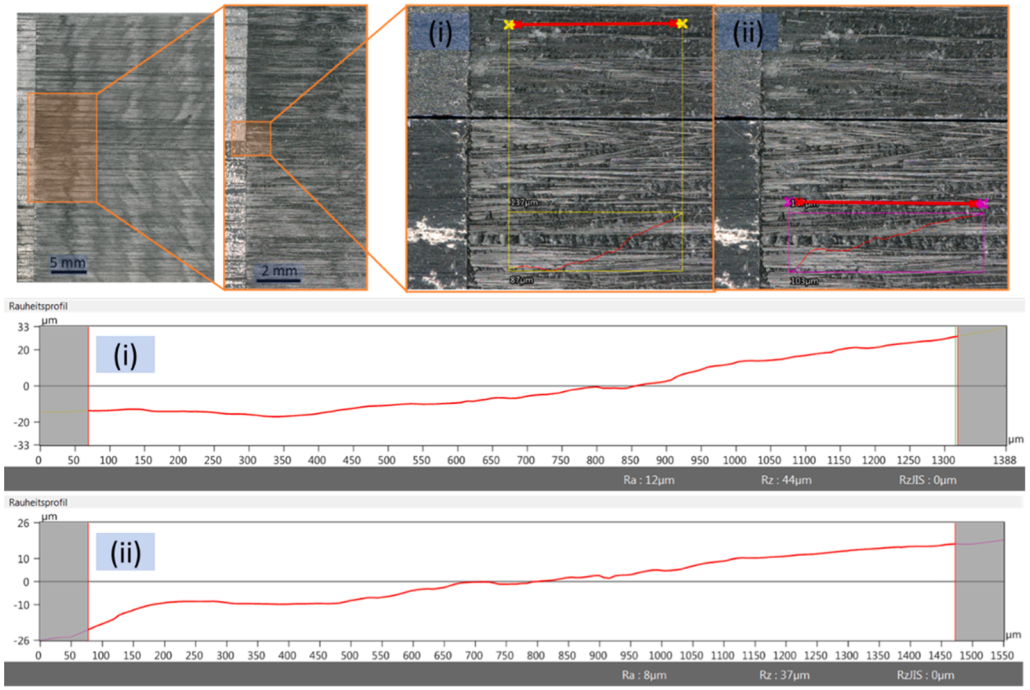

Fig. 9. Roughness of the sample $[0°/+45°/-45°]_{2S}$.

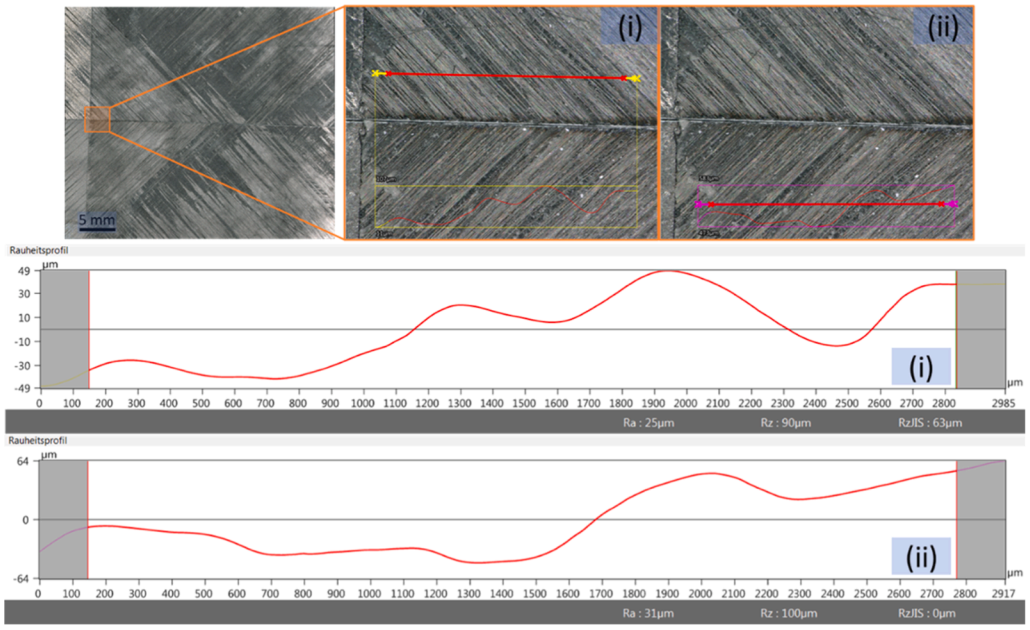

Fig. 10. Roughness of the sample $[+45°/-45°/0°]_{2S}$.

progressive damage development during loading. The 30 mm loading condition shows significantly different behavior, with cumulative AE hits increasing rapidly near the end of the loading period. The sharp rise in the cumulative hit curve indicates the occurrence of intense damage activity associated with crack propagation and delamination growth. This observation is supported by the amplitude distribution, where a dense cluster of AE signals with higher amplitudes appears near the final loading stage. The concentration of these signals suggests that a large amount of elastic energy was released during the sudden crack propagation, consistent with the catastrophic failure behavior observed in the visual crack propagation results.

AE response of the $[+45°/-45°/0°]_{2S}$ laminates under ENF loading with different loading lengths of 20 mm, 30 mm, and 40 mm are shown in Fig. 12. For the 20 mm loading condition, only a small number of AE hits are detected. The cumulative curve remains relatively low, indicating limited internal damage during loading. The corresponding amplitude distribution also shows only a few scattered signals, suggesting that the laminate remains structurally stable with minimal crack development. At the 40 mm loading condition, the cumulative AE hits increase more noticeably, forming several step-like increments that indicate intermittent micro-damage events such as matrix cracking or local interfacial debonding. The amplitude distribution becomes slightly denser compared to the 20 mm case, reflecting increased internal activity as the load progresses.

This behavior suggests the initiation of progressive damage within the laminate structure before reaching the final fracture stage. A significantly different response is observed at the 30 mm loading condition, where the cumulative AE hits increase sharply near the end of the loading period. The rapid rise of AE activity corresponds to intensive damage processes, including crack propagation and delamination growth. The amplitude plot also shows a dense cluster of signals with wider amplitude distribution, indicating a high release of elastic energy during fracture. This result confirms that the [+45°/−45°/0°]2S laminates experience strong acoustic activity associated with progressive damage accumulation and final crack propagation during the ENF test.

Fig. 13 compares the AE characteristics of the $[+45°/-45°/0°]_{2S}$ and $[0°/+45°/-45°]_{2S}$ laminates using several AE parameters, including absolute energy, signal duration, and average frequency. The absolute energy vs. time plots (Fig. 13a) show that both laminates experience low energy release during the early loading stage, followed by a sharp spike near failure, indicating rapid crack propagation and final delamination.

A similar trend is observed in the duration vs. time plots (Fig. 13b), where $[0°/+45°/-45°]_{2S}$ laminates have less crack duration with the peak around 26000µs compared with $[+45°/-45°/0°]_{2S}$ laminates with 35000µs. This indication is consistent with the visual observations presented in Fig. 7 and Fig. 8. The average frequency vs. time plots (Fig. 13c) further support this observation. The $[0°/+45°/-45°]_{2S}$ laminates exhibit longer tests but narrower AE signals prior to failure. The [+45°/−45°/0°]2S laminate shows a denser cluster of signals, with the average frequency sprayed more evenly up to near the final loading stage. This indicates that the $[+45°/-45°/0°]_{2S}$ laminate shows a more pronounced accumulation of AE events before the final energy burst, suggesting a buildup of microcracks prior to catastrophic failure. In contrast, the $[0°/+45°/-45°]_{2S}$ laminate exhibits fewer precursor events before failure.

The AE parameters in the present study are correlated with observed damage evolution, as determined by visual inspection, roughness measurements, and SEM analysis, to provide a more systematic interpretation. The gradual increase in cumulative hits and moderate energy levels observed in the $[+45°/-45°/0°]_{2S}$ laminates is associated with progressive micro-damage accumulation, including interfacial sliding and crack deflection along ±45° plies. This interpretation is supported by the higher surface roughness (Ra ≈ 25–31 µm) and the more tortuous fracture morphology observed in SEM images, both of which indicate enhanced energy dissipation mechanisms. In contrast, the $[0°/+45°/-45°]_{2S}$ laminates exhibit relatively low AE activity before failure, followed by a sudden high-energy burst. This behavior corresponds to delayed crack initiation and unstable crack propagation, as confirmed by visual observation and smoother fracture surfaces (Ra ≈ 8–12 µm). Therefore, the AE response in this configuration reflects a dominant energy storage–release mechanism rather than progressive damage accumulation. It should be noted that specific failure behaviors need to be validated using other methods and are not assigned solely based on AE signal features. This approach ensures a physically consistent interpretation while avoiding overclassification of overlapping AE signals.

3.4. Ultrasonic Lamb wave scanning (ULW) test

The ULW results that detect internal damage in the laminates after testing are shown in Fig. 14. The scans compare the failed specimens of

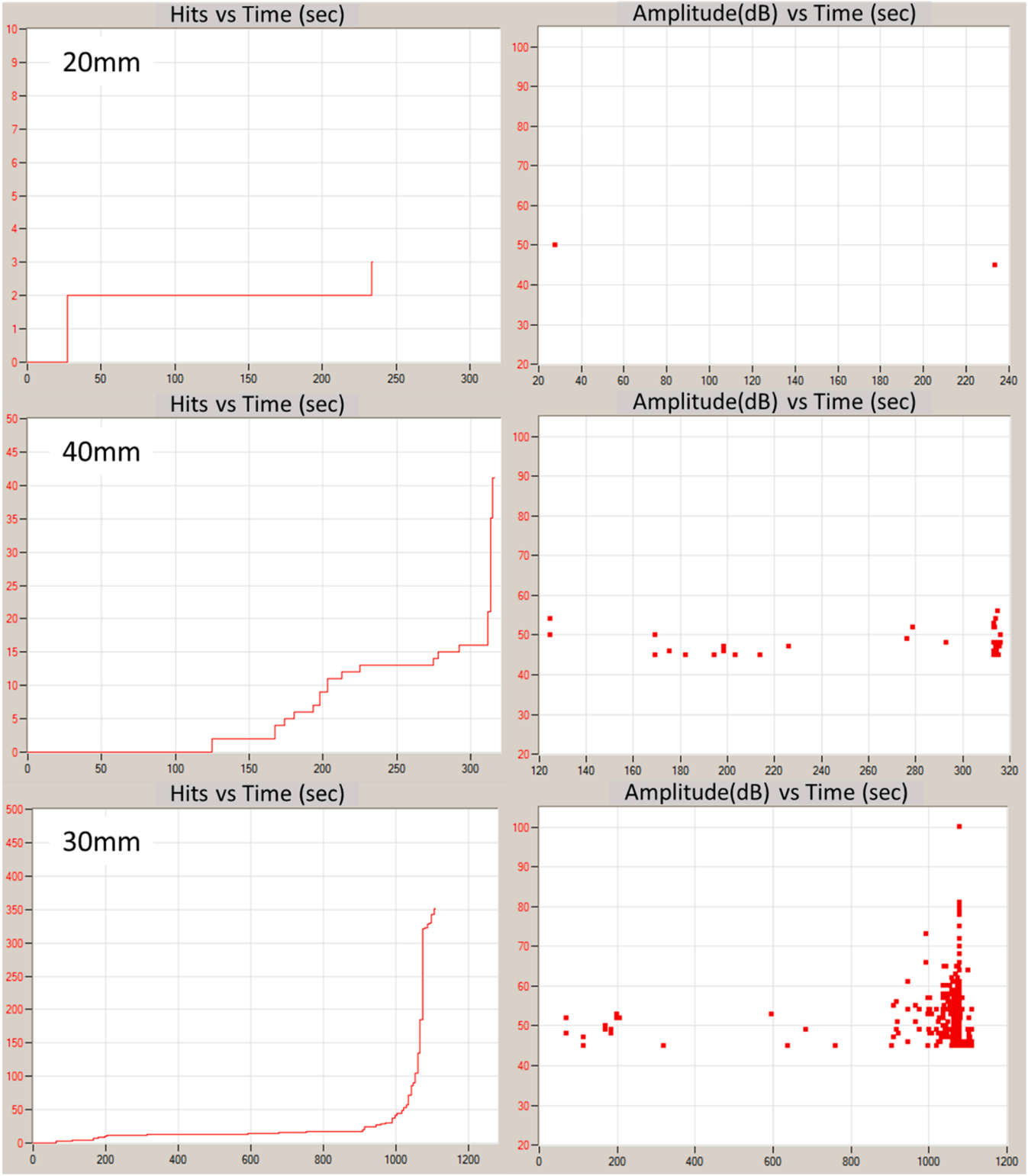

Fig. 11. AE results from $[0°/+45°/-45°]_{2S}$ layup with different length of load.

(a) $[0°/+45°/-45°]_{2S}$ laminates, and (b) $[+45°/-45°/0°]_{2S}$ laminates. The color variation represents the signal response, where changes in the color distribution indicate internal defects or delamination zones within the laminate. In the original specimens, the signal distribution appears relatively uniform, suggesting that the laminates were initially free from significant internal damage. For the $[0°/+45°/-45°]_{2S}$ laminates shown in Fig. 14(a), the failed samples exhibit a wider area of signal variation in the central region of the specimen. The presence of yellow and green zones indicates a larger delaminated area or internal damage caused by crack propagation during the ENF test. This distribution suggests that damage spreads along the interface and affects a broader region around the crack path. In the other sample, $[+45°/-45°/0°]_{2S}$ laminates shown in Fig. 14(b) exhibit a more localized damage pattern. The damage is concentrated near the mid-section, where the crack initiates and

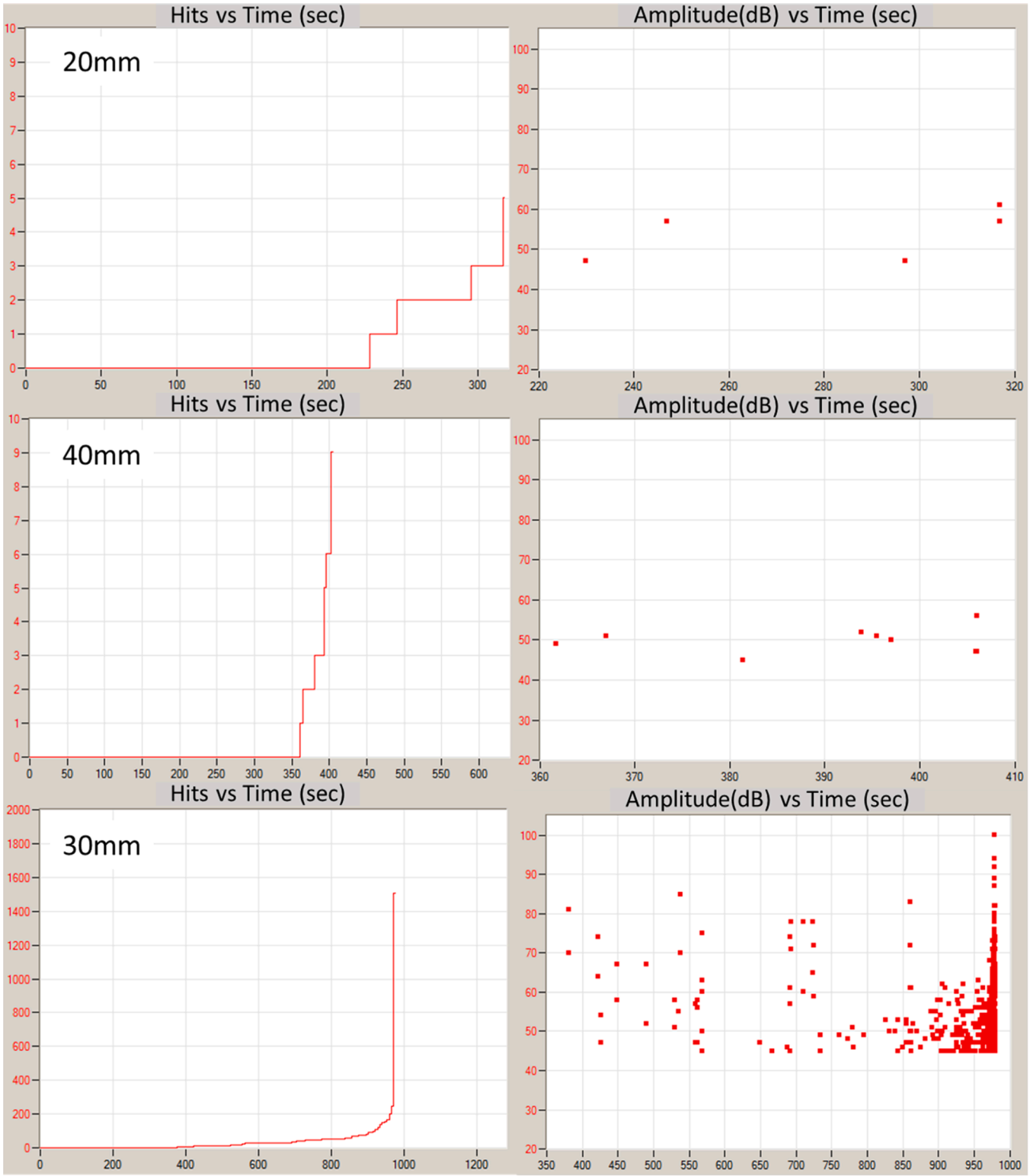

Fig. 12. AE results from $[+45°/-45°/0°]_{2S}$ laminates with different length of load.

propagates, while the surrounding areas remain relatively uniform. This indicates that delamination growth is more confined than the broader damage zone observed in the $[0°/+45°/-45°]_{2S}$ laminates. The ULW results support previous observations from crack propagation and AE analysis, showing that the stacking sequence significantly influences the damage distribution and delamination behavior of the laminate.

4. Discussion with destructive validation

NDT analysis conducted in the present study showed that the laminates exhibit a failure mechanism at different points. $[0°/+45°/-45°]_{2S}$ layups have more silent crack propagation during loading performance but have intense cracking and longer failure length detected, where $[+45°/-45°/0°]_{2S}$ layups exhibited more equal spreading crack along

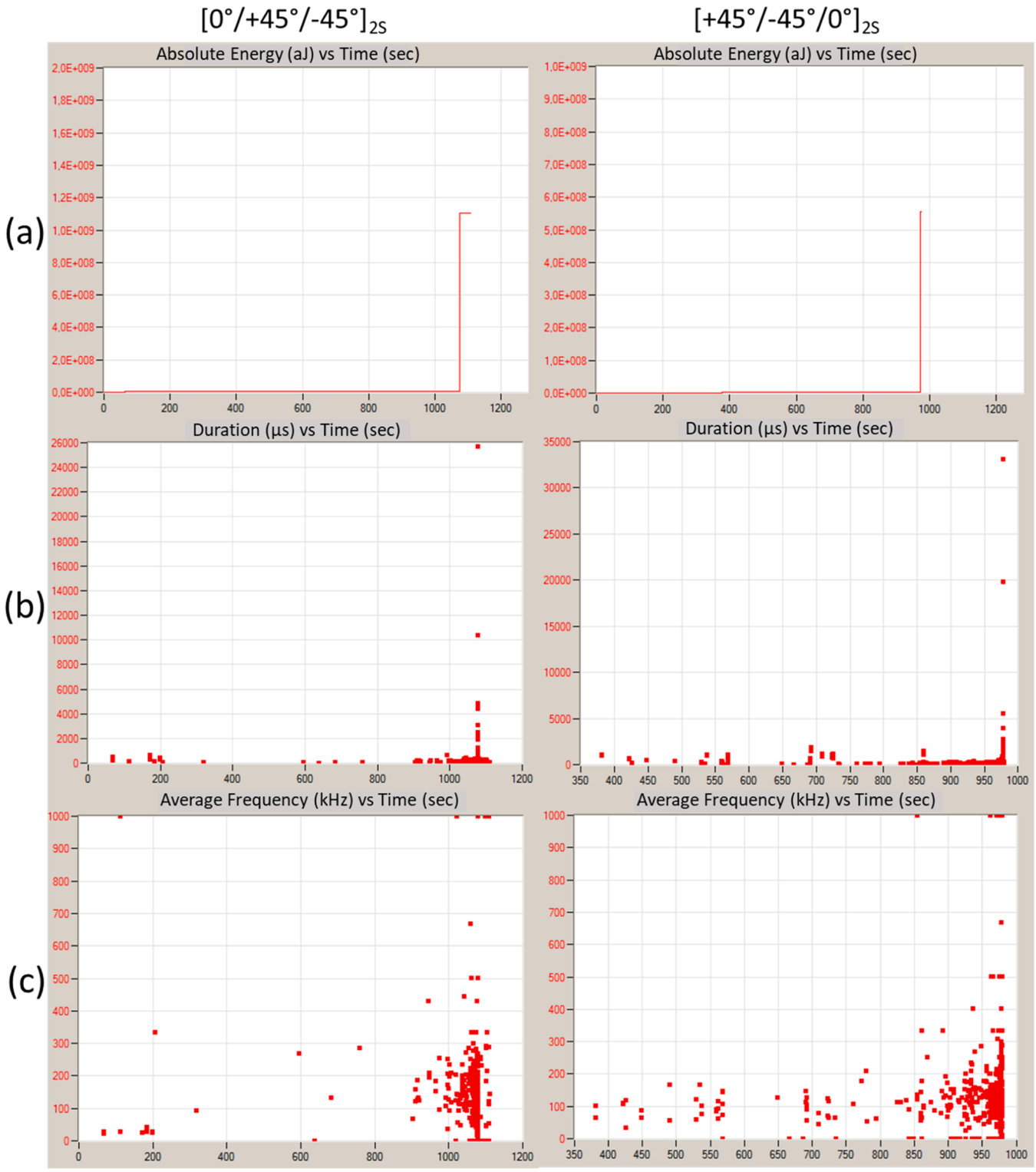

Fig. 13. AE results from $[+45°/-45°/0°]_{2S}$ and $[0°/+45°/-45°]_{2S}$ layup with different parameters. (a) Absolute energy (aJ) vs Time (*sec*), (b) Duration (µs) vs Time (*sec*), (c) Average Frequency (kHz) vs Time (*sec*).

the crack propagation with shorter length, and more intense before final failure. These observations are consistent with previous fracture characterization studies on composite laminates subjected to mode II loading using ENF configurations, where unstable crack propagation and sudden crack growth may occur once the critical fracture resistance is reached [61]. In addition, analytical and numerical investigations on ENF-based fracture tests show that the stacking configuration and stiffness distribution strongly influence the energy release rate and crack-tip stress field, which ultimately control the crack propagation pattern in laminated composites [62]. A similar damage evolution behavior has also been reported in studies investigating the static and fatigue loading of CFRP laminates using non-destructive testing techniques. Ultrasonic inspection combined with Micro-CT analysis shows that fatigue loading leads to the progressive accumulation of internal defects, such as matrix

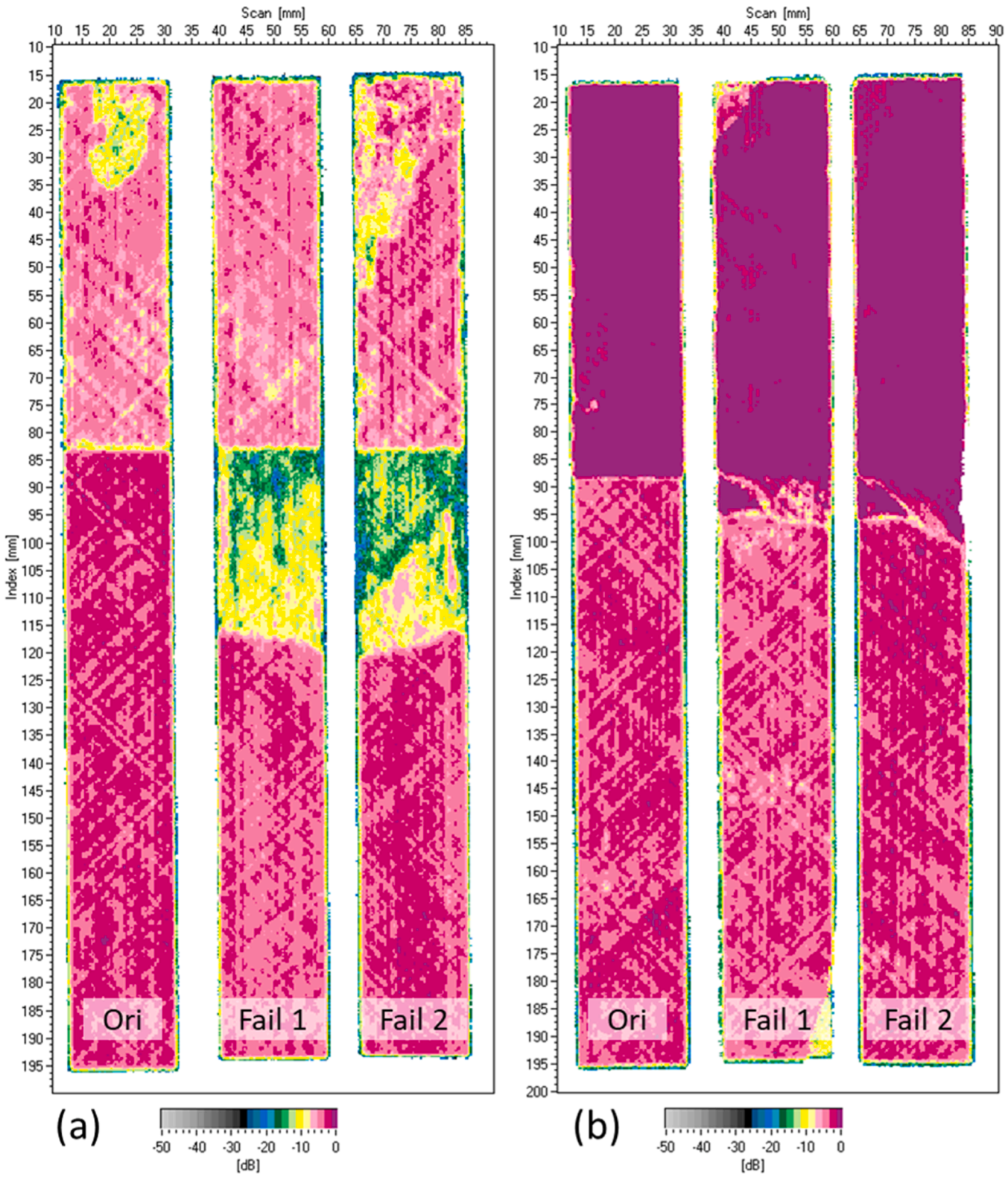

Fig. 14. Ultrasound test on the sample. (a) $[0°/+45°/-45°]_{2S}$, (b) $[+45°/-45°/0°]_{2S}$.

cracking, porosity, and interlaminar delamination, which gradually grow and interact until final failure [63]. Other NDT techniques, including optical methods such as shearography, have also demonstrated high sensitivity in detecting defect-induced deformation and strain anomalies in composite laminates, providing effective full-field monitoring of internal damage [64]. The NDT evaluation obtained in the present study is consistent with previous studies and can effectively identify crack initiation, damage accumulation, and crack propagation behavior in laminated composite structures.

Validation of the study was further analyzed using SEM–EDS and Shore D hardness measurements, as presented in Fig. 15. The SEM–EDS analysis of the $[0°/+45°/-45°]_2S$ laminate in Fig. 15(a) reveals the

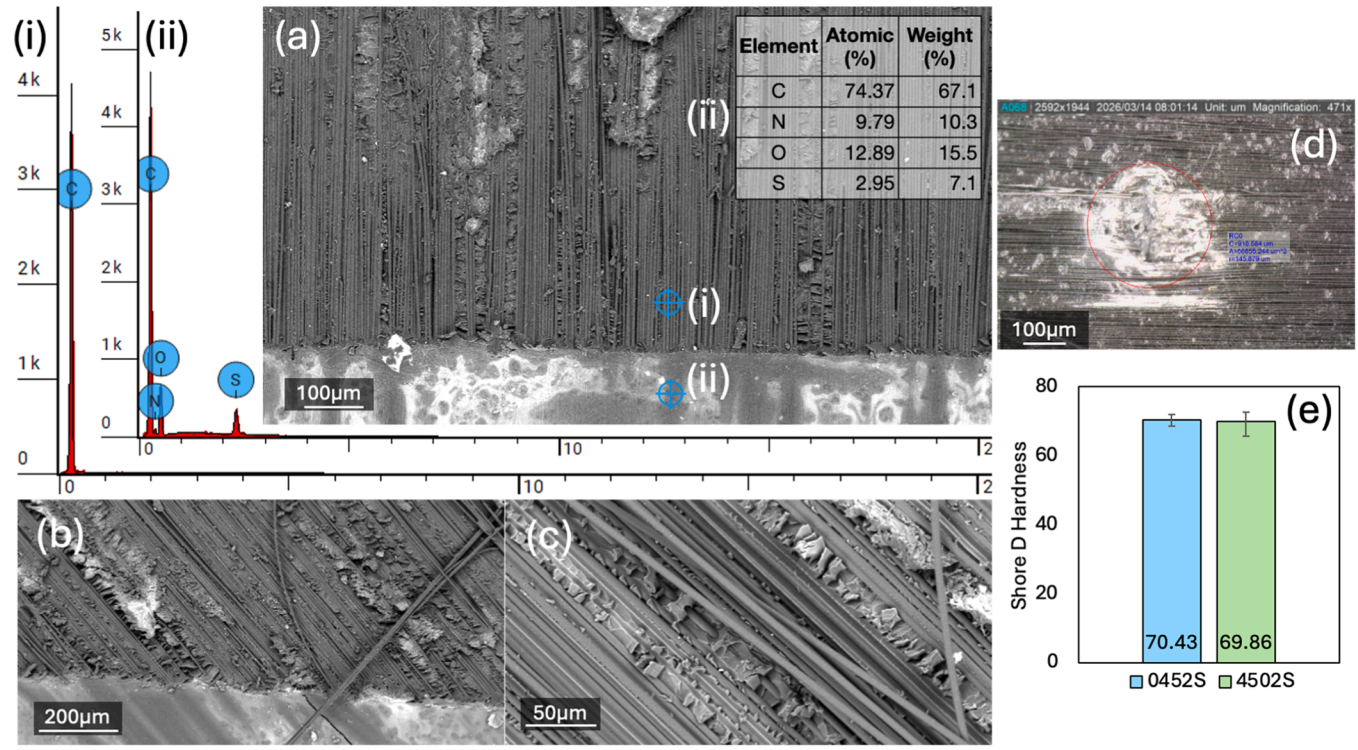

Fig. 15. (a) SEM-EDS of $[0°/+45°/-45°]_{2S}$ layups with the different elements, (b) SEM image from $[+45°/-45°/0°]_{2S}$ layups with 420 magnification, (c) with 1500 magnification, (d) Indentation trace from Shore D hardness, (e) Comparison results from Shore D hardness.

elemental composition dominated by carbon (C), nitrogen (N) and oxygen (O), indicating the presence of polymer matrix and interfacial regions within the composite structure. The SEM micrographs of the $[+45°/-45°/0°]_2S$ laminate shown in Fig. 15(b) and Fig. 15(c) illustrate the fracture surface morphology at magnifications of 420× and 1500×, respectively, where aligned fiber traces and matrix deformation along the fiber direction can be clearly observed, suggesting that the crack propagation tends to follow the fiber–matrix interface and local shear paths under loading. In addition, the indentation trace obtained from Shore D hardness testing in Fig. 15(d) indicates the localized deformation behavior of the composite surface during hardness measurement. The quantitative comparison shown in Fig. 15(e) demonstrates that the Shore D hardness values of both stacking configurations are relatively similar, with 70.43 for $[0°/+45°/-45°]_2S$ and 69.86 for $[+45°/-45°/0°]_2S$ laminates, suggesting that the difference in crack propagation behavior observed in the previous sections is primarily influenced by the stacking sequence and stress distribution rather than by significant differences in surface hardness or matrix properties.

The correlation between surface roughness, fracture morphology, and measured GIIC values provides deeper insight into the underlying energy-dissipation mechanisms governing Mode II delamination. The smoother fracture surface observed in the $[0°/+45°/-45°]_2S$ laminates (Ra ≈ 8–12 μm) indicates a relatively straight crack path dominated by matrix shear failure with minimal crack deflection, which limits energy absorption during propagation. This is consistent with the sudden and unstable crack growth observed in the ENF and AE results, where elastic energy is rapidly released once the critical condition is reached. In contrast, the significantly higher roughness in the $[+45°/-45°/0°]_{2S}$ laminates (Ra ≈ 25–31 μm) reflects a more tortuous crack path induced by the ±45° fiber orientations, promoting mechanisms such as fiber–matrix debonding, crack branching, and local fiber bridging. These mechanisms increase the fracture surface area and enhance frictional sliding at the interface, thereby increasing energy dissipation during crack propagation. Consequently, although the G_{IIC} values of both laminates are relatively close, the slightly higher G_{IIC} in the $[+45°/-45°/0°]_{2S}$ laminates configuration can be physically attributed to these additional micro-mechanisms, which stabilize crack growth and delay catastrophic failure. This relationship highlights that matrix properties do not solely govern fracture toughness in CFRP laminates but are strongly influenced by crack path complexity and interfacial interactions, as dictated by the stacking sequence.

5. Conclusion

The present study investigated the Mode II fracture (G_{IIC}) and damage evolution of CFRP laminates using ENF testing combined with NDT. The findings of this study can be summarized as follows:

- Stacking sequence strongly affects ENF response. $[0°/+45°/-45°]_{2S}$ laminates exhibit higher flexural stiffness and load-carrying capability, with more than two times higher load capacity compared with the $[+45°/-45°/0°]_{2S}$ laminates.
- The G_{IIC} values indicate that both laminates exhibit comparable resistance to delamination. The $[0°/+45°/-45°]_{2S}$ laminates present an average GIIC of 1.70 kJ/m², while the $[+45°/-45°/0°]_{2S}$ laminates show a slightly higher average value of 1.78 kJ/m².
- Visual crack-propagation analysis reveals distinct fracture mechanisms. The $[0°/+45°/-45°]_{2S}$ laminates delay crack initiation but fail catastrophically, while the [+45°/−45°/0°]2S laminates initiate cracks earlier, with more stable propagation before final failure.
- Surface roughness analysis confirms that the laminates differ according to the ply orientation. The $[0°/+45°/-45°]_{2S}$ laminates are smoother (Ra ~8–12 μm; Rz ~37–44 μm, more brittle), while the $[+45°/-45°/0°]_{2S}$ laminates are rougher (Ra ~25–31 μm; Rz ~90–100 μm) due to crack deflection and fiber–matrix debonding.
- AE monitoring shows distinct damage evolution. The $[0°/+45°/-45°]_{2S}$ laminates show minimal precursor signals followed by a sudden high-energy burst (catastrophic failure), while the $[+45°/-45°/0°]_{2S}$ laminates exhibit gradual AE accumulation, indicating progressive micro-damage.

- ULW effectively maps post-ENF delamination. The $[0°/+45°/-45°]_{2S}$ laminates display a wider delamination zone, while the $[+45°/-45°/0°]_{2S}$ laminates exhibit a more localized damage near the crack path.
- SEM–EDS confirms that a carbon-based matrix with aligned fibers and matrix deformation dominates the fracture.
- Shore D hardness values are nearly identical for both laminates (70.43 for $[0°/+45°/-45°]_{2S}$ and 69.86 for $[+45°/-45°/0°]_{2S}$), indicating that fracture differences are governed by stacking sequence and stress distribution, not matrix hardness.

From an engineering perspective, the integration of AE and ULW enables reliable differentiation between catastrophic and progressive failure modes, supporting SHM development for aerospace composites; however, this study is limited to quasi-static ENF loading, room temperature, and two stacking sequences, and future work should address fatigue and impact loading, environmental effects, broader stacking configurations, and real-time evaluation for predictive maintenance.

CRediT authorship contribution statement

Muhammad Akhsin Muflikhun: Writing – review & editing, Writing – original draft, Visualization, Validation, Software, Methodology, Investigation, Formal analysis, Data curation, Conceptualization. **Bodo Fiedler:** Writing – review & editing, Writing – original draft, Visualization, Supervision, Resources, Project administration, Funding acquisition, Conceptualization.

Declaration of competing interest

The authors declare that they have no known competing financial interests or personal relationships that could have appeared to influence the work reported in this paper.

Acknowledgements

The authors would like to thank TU Hamburg and UGM for the collaboration on this research.

Data availability

Data will be made available on request.

References

[1] K.N. Antin, M.A. Machado, T.G. Santos, P. Vilaça, Evaluation of different non-destructive testing methods to detect imperfections in unidirectional carbon Fiber composite ropes, J. Nondestr. Eval. 38 (2019) 1–12, https://doi.org/10.1007/s10921-019-0564-y.

[2] M.A. Muflikhun, T. Yokozeki, T. Aoki, The strain performance of thin CFRP-SPCC hybrid laminates for automobile structures, Compos. Struct. 220 (2019) 11–18, https://doi.org/10.1016/j.compstruct.2019.03.094.

[3] F.E. Yakin, C.O. Senol, N. Birgün, H. Ulus, M. Yildiz, H.S. Sas, Influence of stacking sequence and compaction force during the AFP process on mechanical performance and damage mechanisms elucidated by acoustic emission insights, Proc. Inst. Mech. Eng. L: J. Mater.: Des. Appl. 240 (2026) 19–34.

[4] G. Tefera, G. Bright, S. Adali, Flexural and shear properties of CFRP laminates reinforced with functionalized multiwalled CNTs, Nanocomposites 7 (2021) 141–153, https://doi.org/10.1080/20550324.2021.1961507.

[5] Y. Ou, A. Fu, L. Wu, X. Yi, D. Mao, Enhanced interlaminar fracture toughness of unidirectional CFRP laminates with tailored microstructural heterogeneity of toughening layer, Compos. Appl. Sci. Manuf. 176 (2024) 107872, https://doi.org/10.1016/j.compositesa.2023.107872.

[6] H. Ulus, M.E. Çetin, B. Beylergil, H.B. Kaybal, Quasi-static and thermoviscoelastic response of carbon/epoxy–Aluminum FMLs: effects of stacking sequence and graphene–TiO_2 nano-modification, Fibers Polym. 27 (2026) 2463–2484, https://doi.org/10.1007/s12221-026-01371-2.

[7] H. Senol, H. Ulus, A. Al-Nadhari, S. Topal, M. Yildiz, Ameliorating tensile and fracture performance of carbon fiber-epoxy composites via atmospheric plasma activation: insights into damage modes through in-situ acoustic emission inspection, Compos. Appl. Sci. Manuf. 195 (2025) 108929, https://doi.org/10.1016/j.compositesa.2025.108929.

[8] C. Barile, C. Casavola, G. Pappalettera, Acoustic emission waveform analysis in CFRP under mode I test, Eng. Fract. Mech. 210 (2019) 408–413, https://doi.org/10.1016/j.engfracmech.2018.01.023.

[9] J. Chen, Z. Yu, H. Jin, Non-destructive testing and evaluation techniques of defects in fiber-reinforced polymer composites: a review, Front. Mater. 9 (2022), https://doi.org/10.3389/fmats.2022.986645.

[10] M.A. Muflikhun, B. Fiedler, Comprehensive evaluation of CFRP laminates using NDT methods for aircraft applications, J. Mater. Res. Technol. 32 (2024) 395–409, https://doi.org/10.1016/j.jmrt.2024.07.196.

[11] J. Liu, Y. Li, D. Xiang, C. Zhao, B. Wang, H. Li, Enhanced electrical conductivity and interlaminar fracture toughness of CF/EP composites via interleaving conductive thermoplastic films, Appl. Compos. Mater. 28 (2021) 17–37, https://doi.org/10.1007/s10443-020-09848-w.

[12] G. Zhao, X. Zhang, W. Qiang, X. Zhang, Enhancing the interlaminar toughness and impact resistance of CFRP using MWCNTs and core-shell rubber synergistic strategy, Thin-Walled Struct. 212 (2025) 113146, https://doi.org/10.1016/j.tws.2025.113146.

[13] V. Dattoma, F.W. Panella, A. Pirinu, A. Saponaro, Advanced NDT methods and data processing on industrial CFRP components, Appl. Sci. (Switz.) 9 (2019) 393, https://doi.org/10.3390/app9030393.

[14] S. Oshima, A. Mamishin, M. Hojo, M. Nishikawa, N. Matsuda, M. Kanesaki, High-resolution in situ characterization of micromechanisms in CFRP laminates under mode II loading, Eng. Fract. Mech. 260 (2022) 108189, https://doi.org/10.1016/j.engfracmech.2021.108189.

[15] S. Han, Q. Li, Z. Cui, P. Xiao, Y. Miao, L. Chen, et al., Non-destructive testing and structural health monitoring technologies for carbon fiber reinforced polymers: a review, Non-destr. Test. Eval. 39 (2024) 725–761, https://doi.org/10.1080/10589759.2024.2324149.

[16] D.S.V. de Castro, N. Matvieieva, M. Grosso, C.G. Camerini, H.G. Kotik, H. Heuer, Evaluation of mode II delamination area by non-destructive techniques: accuracy and influence on fracture toughness calculation, J. Nondestr. Eval. 40 (2021), https://doi.org/10.1007/s10921-021-00789-3.

[17] X. Zou, L. Wang, J. Wang, J. Liu, H. Ma, Y. Bao, Non-destructive evaluation of carbon fiber reinforced polymer (CFRP)-steel interfacial debonding using eddy current thermography, Compos. Struct. 284 (2022) 115133, https://doi.org/10.1016/j.compstruct.2021.115133.

[18] L.B. Andraju, G. Raju, Damage characterization of CFRP laminates using acoustic emission and digital image correlation: clustering, damage identification and classification, Eng. Fract. Mech. 277 (2023) 108993, https://doi.org/10.1016/j.engfracmech.2022.108993.

[19] Y. Zhu, W. Li, J. Lin, F. Gao, Z. Liu, A multi-mode coupling damage classification method for composite structures based on acoustic emission signal decomposition, Ultrasonics 160 (2026) 107886, https://doi.org/10.1016/j.ultras.2025.107886.

[20] B. Wang, W. Shi, B. Zhao, J. Tan, A modal decomposition imaging algorithm for ultrasonic detection of delamination defects in carbon fiber composite plates using air-coupled Lamb waves, Meas. (L.) 195 (2022) 111165, https://doi.org/10.1016/j.measurement.2022.111165.

[21] J. Jodhani, A. Handa, A. Gautam, Ashwni, R. Rana, Ultrasonic non-destructive evaluation of composites: a review, Mater. Today Proc. 78 (2023) 627–632, https://doi.org/10.1016/j.matpr.2022.12.055. Elsevier Ltd.

[22] S. Akgun, C.O. Senol, G. Kilic, I.E. Tabrizi, M. Yildiz, A novel damage evaluation of CFRPs under mode-I loading by using multi-instrument structural health monitoring methods, Eng. Fract. Mech. 286 (2023) 109291, https://doi.org/10.1016/j.engfracmech.2023.109291.

[23] T.L.L. Oliveira, D.B. Bortoluzzi, L.C.M. Barbosa, A.C. Ancelotti, Acoustic emission analysis of mode II interlaminar fracture toughness of 3D reinforced CFRP, NDT 2 (2024) 32–52, https://doi.org/10.3390/ndt2010003.

[24] R.A.A. Lima, R. Tao, A. Bernasconi, M. Carboni, S. Teixeira de Freitas, Acoustic emission approach for identifying fracture mechanisms in composite bonded joints: a study on varying Substrate's stacking sequence, Theor. Appl. Fract. Mech. 132 (2024) 104490, https://doi.org/10.1016/j.tafmec.2024.104490.

[25] Y. Gong, K. Xia, Y. Wang, L. Zhao, J. Zhang, N. Hu, A semi-analytical model for the mode II fracture toughness of multidirectional composite laminates, Thin-Walled Struct. 182 (2023) 110235, https://doi.org/10.1016/j.tws.2022.110235.

[26] S.S. Khedmatgozar Dolati, P. Malla, J.D. Ortiz, A. Mehrabi, A. Nanni, Identifying NDT methods for damage detection in concrete elements reinforced or strengthened with FRP, Eng. Struct. 287 (2023) 116155, https://doi.org/10.1016/j.engstruct.2023.116155.

[27] P. Golewski, T. Sadowski, M. Kneć, M. Budka, The effect of thermal aging degradation of CFRP composite on its mechanical properties using destructive and non-destructive methods and the DIC system, Polym. Test. 118 (2023) 107902, https://doi.org/10.1016/j.polymertesting.2022.107902.

[28] A.D. Nugraha, D. Alandro, K.G.H. Mangunkusumo, M. Kusni, Y.C. Wu, M. A. Muflikhun, Failure configuration and evaluation of hybrid CFRP-GFRP laminates using innovative Arcan fixture: experimental and simulation approach, Compos. C: Open Access 14 (2024) 100452, https://doi.org/10.1016/j.jcomc.2024.100452.

[29] W. Feng, M.M. Arouche, M. Pavlovic, Fatigue crack growth characterization of composite-to-steel bonded interface using ENF and 4ENF tests, Compos. Struct. 334 (2024) 117963, https://doi.org/10.1016/j.compstruct.2024.117963.

[30] M.F.S.F. de Moura, R.D.F. Moreira, F.M.G. Ramírez, Influence of geometric and material parameters on the mode II interlaminar fatigue/fracture characterization of CFRP laminates, Compos. Sci. Technol. 210 (2021) 108819, https://doi.org/10.1016/j.compscitech.2021.108819.

[31] Q.Q. Ni, J. Hong, P. Xu, Z. Xu, K. Khvostunkov, H. Xia, Damage detection of CFRP composites by electromagnetic wave non-destructive testing (EMW-NDT), Compos.

Sci. Technol. 210 (2021) 108839, https://doi.org/10.1016/j.compscitech.2021.108839.
[32] M.A. Machado, K.N. Antin, L.S. Rosado, P. Vilaça, T.G. Santos, High-speed inspection of delamination defects in unidirectional CFRP by non-contact eddy current testing, Compos. B Eng. 224 (2021) 109167, https://doi.org/10.1016/j.compositesb.2021.109167.
[33] R. Zhang, J. Wang, S. Liu, M. Ma, H. Fang, J. Cheng, et al., Non-destructive testing of carbon fibre reinforced plastics (CFRP) using a dual transmitter-receiver differential eddy current test probe, Sensors 22 (2022) 6761, https://doi.org/10.3390/s22186761.
[34] M. Ma, S. Liu, R. Zhang, Q. Zhang, Y. Wu, B. Chen, Non-destructive testing of carbon Fiber-reinforced plastics (CFRPs) using a resonant eddy current sensor, Sensors 24 (2024) 3449, https://doi.org/10.3390/s24113449.
[35] A.I. Moskovchenko, V.P. Vavilov, A.O. Chulkov, Comparing the efficiency of defect depth characterization algorithms in the inspection of CFRP by using one-sided pulsed thermal NDT, Infrared. Phys. Technol. 107 (2020) 103289, https://doi.org/10.1016/j.infrared.2020.103289.
[36] V. Rodríguez-García, M. Herráez, V. Martínez, R. Guzman de Villoria, Interlaminar and translaminar fracture toughness of automated manufactured bio-inspired CFRP laminates, Compos. Sci. Technol. 219 (2022) 109236, https://doi.org/10.1016/j.compscitech.2021.109236.
[37] Y. Liu, A. Zou, G.Dong Wang, C. Han, E. Blackie, Enhancing interlaminar fracture toughness of CFRP laminates with hybrid carbon nanotube/graphene oxide fillers, Diam. Relat. Mater. 128 (2022) 109285, https://doi.org/10.1016/j.diamond.2022.109285.
[38] J. Koord, O. Völkerink, E. Petersen, C. Hühne, Effect of low temperature on mode I and mode II interlaminar fracture toughness of CFRP-steel hybrid laminates, Compos. B Eng. 262 (2023) 110773, https://doi.org/10.1016/j.compositesb.2023.110773.
[39] A.S.D. Al-Ridha, K.S. Mahmoud, A.F Atshan, Effect of carbon fiber reinforced polymer (CFRP) laminates on behaviour of flexural strength of steel beams with and without end anchorage plates. Mater, Today Proc. 49 (2022) 2778–2785, https://doi.org/10.1016/j.matpr.2021.09.313. Elsevier Ltd.
[40] J. Rzeczkowski, An experimental analysis of the end-notched flexure composite laminates beams with elastic couplings, Contin. Mech. Thermodyn. 33 (2021) 2331–2343, https://doi.org/10.1007/s00161-020-00903-2.
[41] M.A. Muflikhun, T. Yokozeki, Systematic analysis of fractured specimens of composite laminates: different perspectives between tensile, flexural, mode I, and mode II test, Int. J. Lightweight Mater. Manuf. 6 (2023) 329–343, https://doi.org/10.1016/j.ijlmm.2023.03.003.
[42] Q. Sourisseau, E. Lepretre, S. Chataigner, X. Chapeleau, L. Mouton, S. Paboeuf, Use of high spatial resolution distributed optical fiber to monitor the crack propagation of an adhesively bonded joint during ENF and DCB tests, Int. J. Adhes. Adhes. 115 (2022) 103124, https://doi.org/10.1016/j.ijadhadh.2022.103124.
[43] M. Tauheed, N.V Datla, Characterization and prediction of hygrothermally aged CFRP adhesive joint subjected to mode II load, Compos. C: Open Access 11 (2023) 100357, https://doi.org/10.1016/j.jcomc.2023.100357.
[44] F. Yang, F. Yi, W. Xie, The role of ply angle in interlaminar delamination properties of CFRP laminates, Mech. Mater. 160 (2021) 103928, https://doi.org/10.1016/j.mechmat.2021.103928.
[45] S. Oshima, A. Yoshimura, Y. Hirano, T. Ogasawara, K.T. Tan, In-situ observation of microscopic damage in adhesively bonded CFRP joints under mode I and mode II loading, Compos. Struct. 227 (2019) 111330, https://doi.org/10.1016/j.compstruct.2019.111330.
[46] A. Gliszczynski, N. Wiącek, Experimental and numerical benchmark study of mode II interlaminar fracture toughness of unidirectional GFRP laminates under shear loading using the end-notched flexure (ENF) test, Compos. Struct. 258 (2021) 113190, https://doi.org/10.1016/j.compstruct.2020.113190.
[47] R. Mohammadi, M. Ahmadi Najafabadi, H. Saghafi, M. Saeedifar, D. Zarouchas, A quantitative assessment of the damage mechanisms of CFRP laminates interleaved by PA66 electrospun nanofibers using acoustic emission, Compos. Struct. 258 (2021) 113395, https://doi.org/10.1016/j.compstruct.2020.113395.
[48] M.F. Abd Rased, S.H Yoon, Experimental study on effects of asymmetrical stacking sequence on carbon fiber/epoxy filament wound specimens in DCB, ENF, and MMB tests, Compos. Struct. 264 (2021) 113749, https://doi.org/10.1016/j.compstruct.2021.113749.
[49] R. Sako, R. Aoki, R. Higuchi, M. Ueda, Y. Urushiyama, T. Yokozeki, Experiments on the mode II fracture toughness in ENF tests of CFRP curved beams, Compos. Struct. 292 (2022) 115692, https://doi.org/10.1016/j.compstruct.2022.115692.
[50] W. Dehui, Y. Fan, W. Teng, C. Wenxiong, A novel electromagnetic non-destructive testing method for carbon fiber reinforced polymer laminates based on power loss, Compos. Struct. 276 (2021) 114421, https://doi.org/10.1016/j.compstruct.2021.114421.
[51] W. Li, G. Palardy, Damage monitoring methods for fiber-reinforced polymer joints: a review, Compos. Struct. 299 (2022) 116043, https://doi.org/10.1016/j.compstruct.2022.116043.
[52] L.G. Aryaswara, M. Kusni, D. Wijanarko, M.A. Muflikhun, Advanced properties and failure characteristics of hybrid GFRP-matrix thin laminates modified by micro glass powder filler for hard structure applications, J. Eng. Res. 13 (2025) 142–155, https://doi.org/10.1016/j.jer.2023.08.022.
[53] J. Wang, W. Zhou, X Ying Ren, M Ming Su, J. Liu, A waveform-based clustering and machine learning method for damage mode identification in CFRP laminates, Compos. Struct. 312 (2023) 116875, https://doi.org/10.1016/j.compstruct.2023.116875.
[54] F. Abdollahi-Mamoudan, C. Ibarra-Castanedo, X.P.V. Maldague, Non-destructive testing and evaluation of hybrid and advanced structures: a comprehensive review of methods, applications, and emerging trends, Sensors 25 (2025) 3635, https://doi.org/10.3390/s25123635.
[55] I. Alqurashi, N. Alver, U. Bagci, F.N. Catbas, A review of ultrasonic testing and evaluation methods with applications in civil NDT/E, J. Nondestr. Eval. 44 (2025), https://doi.org/10.1007/s10921-025-01190-0.
[56] S. Han, Q. Li, Z. Cui, P. Xiao, Y. Miao, L. Chen, et al., Non-destructive testing and structural health monitoring technologies for carbon fiber reinforced polymers: a review, Non-destr. Test. Eval. 39 (2024) 725–761, https://doi.org/10.1080/10589759.2024.2324149.
[57] HexPly ® M21. 2020.
[58] S. Psarras, R. Muñoz, M. Ghajari, Compression performance of composite plates after multi-site impacts: a combined experimental and finite element study, Compos. Struct. 322 (2023) 117342, https://doi.org/10.1016/j.compstruct.2023.117342.
[59] L. Wan, Y. Ismail, Y. Sheng, K. Wu, D. Yang, Progressive failure analysis of CFRP composite laminates under uniaxial tension using a discrete element method, J. Compos. Mater. 55 (2021) 1091–1108, https://doi.org/10.1177/0021998320961460.
[60] M.A. Muflikhun, T. Yokozeki, Steel plate cold commercial - carbon fiber reinforce plastics hybrid laminates for automotive applications: curing perspective with thermal residual effect, J. Mater. Res. Technol. 14 (2021) 2700–2714, https://doi.org/10.1016/j.jmrt.2021.07.152.
[61] J.P. Reis, M.F.S.F. de Moura, R.D.F. Moreira, Extension of the crack equivalent method applied to mode II fracture of thermoplastic composites bonded joints using the ENF test, Compos. Struct. 352 (2025) 118687, https://doi.org/10.1016/j.compstruct.2024.118687.
[62] J. Bonhomme, V. Mollón, Finite element analysis of the asymmetric ENF test specimen, Eng. Fract. Mech. 327 (2025) 111504, https://doi.org/10.1016/j.engfracmech.2025.111504.
[63] T. Zheng, Z. Liu, Y. Yin, Q. Gao, T. Jin, Y. Shu, Numerical simulation study on ultrasonic testing for fatigue damage characteristics of CFRP laminates based on Micro-CT, NDT and E Int. 156 (2025) 103466, https://doi.org/10.1016/j.ndteint.2025.103466.
[64] N. Tao, A.G. Anisimov, R.M. Groves, Shearography non-destructive testing of thick GFRP laminates: numerical and experimental study on defect detection with thermal loading, Compos. Struct. 282 (2022) 115008, https://doi.org/10.1016/j.compstruct.2021.115008.